

1 **The Autophagy Receptor NBR1 Directs the Clearance of Photodamaged Chloroplasts**

2

3 Han Nim Lee<sup>1,2</sup>, Jenu Varghese Chacko<sup>1</sup>, Ariadna Gonzalez Solís<sup>1,2</sup>, Kuo-En Chen<sup>3</sup>, Jessica  
4 Barros<sup>3</sup>, Santiago Signorelli<sup>4,5</sup>, A. Harvey Millar<sup>4</sup>, Richard D. Vierstra<sup>3</sup>, Kevin W. Eliceiri<sup>1,6,7,8</sup>, and  
5 Marisa S. Otegui<sup>1,2,\*</sup>

6

7 <sup>1</sup> Center for Quantitative Cell Imaging, University of Wisconsin-Madison, Madison, Wisconsin,  
8 USA.

9 <sup>2</sup> Department of Botany, University of Wisconsin-Madison, Madison, Wisconsin, USA.

10 <sup>3</sup> Department of Biology, Washington University in St. Louis, St. Louis, Missouri, USA.

11 <sup>4</sup> ARC Centre of Excellence in Plant Energy Biology, School of Molecular Sciences, The  
12 University of Western Australia, Perth, West Australia, Australia.

13 <sup>5</sup> Department of Plant Biology, School of Agronomy, Universidad de la República, Montevideo  
14 Uruguay.

15 <sup>5</sup> Department of Medical Physics, University of Wisconsin-Madison, Madison, Wisconsin, USA.

16 <sup>7</sup> Department of Biomedical Engineering, University of Wisconsin-Madison, Madison, Wisconsin,  
17 USA

18 <sup>8</sup> Morgridge Institute for Research, Madison, Wisconsin, USA.

19

20 \* Corresponding author: Marisa S. Otegui; otegui@wisc.edu

21 **Abstract**

22 The ubiquitin-binding NBR1 autophagy receptor plays a prominent role in recognizing  
23 ubiquitylated protein aggregates for vacuolar degradation by macroautophagy. Here, we show  
24 that upon exposing Arabidopsis plants to intense light, NBR1 associates with photodamaged  
25 chloroplasts independently of ATG7, a core component of the canonical autophagy machinery.  
26 NBR1 coats both the surface and interior of chloroplasts, which is then followed by direct  
27 engulfment of the organelles into the central vacuole via a microautophagy-type process. The  
28 relocalization of NBR1 into chloroplasts does not require the chloroplast translocon complexes  
29 embedded in the envelope but is instead greatly enhanced by removing the self-oligomerization  
30 mPB1 domain of NBR1. The delivery of NBR1-decorated chloroplasts into vacuoles depends  
31 on the ubiquitin-binding UBA2 domain of NBR1 but is independent of the ubiquitin E3 ligases  
32 SP1 and PUB4, known to direct the ubiquitylation of chloroplast surface proteins. Compared to  
33 wild-type plants, *nbr1* mutants have altered levels of a subset of chloroplast proteins and display  
34 abnormal chloroplast density and sizes upon high light exposure. We postulate that, as  
35 photodamaged chloroplasts lose envelope integrity, cytosolic ligases reach the chloroplast  
36 interior to ubiquitylate thylakoid and stroma proteins which are then recognized by NBR1 for  
37 autophagic clearance. This study uncovers a new function of NBR1 in the degradation of  
38 damaged chloroplasts by microautophagy.

39

40 Keywords: NBR1, chlorophagy, microautophagy, ubiquitin.

## 41 Introduction

42 Autophagy is a process by which cytoplasmic contents including organelles, individual proteins,  
43 protein complexes and cytosolic aggregates, collectively called autophagic cargo, are delivered  
44 to vacuoles (plants and yeast) and lysosomes (animals) for degradation (Mizushima et al.,  
45 1998). In plants, autophagy most commonly occurs through the formation of cargo-  
46 sequestering double-membrane-bound organelles called autophagosomes (macroautophagy) or  
47 through the direct engulfment of cargo by the vacuolar membrane (microautophagy). Whereas  
48 the molecular underpinnings of microautophagy are poorly understood, the machinery for  
49 macroautophagy involves more than 40 ATG (Autophagy Related) proteins whose actions are  
50 regulated by upstream phosphorylation events ultimately leading to formation of  
51 autophagosomes decorated with a conjugate of ATG8 with phosphatidylethanolamine (PE) (Xie  
52 et al., 2008). This conjugation is mediated an enzymatic cascade sequentially involving the  
53 activating enzyme ATG7, the conjugating enzyme ATG3, and a ligase complex comprising an  
54 ATG5-ATG12 conjugate complexed with ATG16 (Ohsumi, 2001). The resulting ATG8-PE  
55 adduct is not only required for autophagosomes assembly but also, through its interaction with a  
56 host of autophagic receptors, for the selection of appropriate autophagic cargo (Noda et al.,  
57 2008).

58 There are several selective autophagy receptors that specifically recognize ubiquitylated  
59 cargo. Among them, metazoan SQSTM1/p62 (Sequestosome 1) and NBR1 (NEIGHBOR OF  
60 BRCA1 gene 1) promote the accretion of ubiquitylated proteins into larger condensates which  
61 are then encapsulated by autophagosomes for macroautophagic clearance (aggrephagy)  
62 (Bjørkøy et al., 2005; Komatsu et al., 2007; Nezis et al., 2008; Turco et al., 2021; Rasmussen et  
63 al., 2022). The PB1 (Phox and Bem1 domain) domain present in both SQSTM1 and NBR1  
64 mediate their mutual interaction and oligomerization into helical filaments (Ciuffa et al., 2015)  
65 which then promote the aggregation of ubiquitylated species (Jakobi et al., 2020; Turco et al.,  
66 2021). In addition, mammalian SQSTM1 and NBR1 share a zinc-finger domain (ZZ) that can  
67 bind N-terminally arginylated proteins, lysine-48 (K48)- and K63-linked polyubiquitylated  
68 proteins, and other cargo (Cha-Molstad et al., 2015; Kwon et al., 2018; Wang et al., 2021), a  
69 ubiquitin-associated (UBA) domain with affinity for ubiquitin, and an ATG8-interacting motif  
70 (AIM) sequence that binds ATG8 (Seibenhener et al., 2004; Ichimura et al., 2008; Zientara-  
71 Rytter et al., 2011; Sun et al., 2022a). NBR1, but not SQSTM1, also contains a Four-  
72 Tryptophan (FW) domain, which at least in some fungal species recognizes cargo for selective  
73 autophagy. The plant NBR1 proteins uniquely harbor two UBA domains but only the C-terminal

74 sequence (UBA2) binds ubiquitin (Svenning et al., 2011). Through these collective features,  
75 SQSTM1 and NBR1 can mediate selective autophagy of cargo in both ubiquitin and ubiquitin-  
76 independent manners. Most non-metazoan species encode only NBR1, whereas metazoans  
77 can express either or both SQSTM1 and NBR1 (Svenning et al., 2011).

78 In plants, NBR1 has been connected genetically to numerous physiological processes  
79 (Zhang and Chen, 2020). For example, it modulates tolerance to heat stress through at least  
80 two mechanisms; recognition and sorting for degradation of proteotoxic ubiquitylated  
81 aggregates that accumulate at high temperatures (Zhou et al., 2013; Zhou et al., 2014), and the  
82 negative regulation of heat stress memory by mediating the clearance of heat-shock-related  
83 chaperones and their co-factors (Thirumalaikumar et al., 2021). Arabidopsis NBR1 also targets  
84 for autophagic clearance: (i) the exocyst subunit EXO70E2 and its associated organelle EXO  
85 (Ji et al., 2020), (ii) misfolded protein aggregates (Jung et al., 2020), and (iii) viral capsid  
86 proteins (Hafren et al., 2017) and pathogenic bacterial effectors (Dagdas et al., 2016; Dagdas et  
87 al., 2018; Üstün et al., 2018; Leong et al., 2022). Remarkably, Arabidopsis null *nbr1* mutants  
88 develop normally under favorable growth conditions and are still able to execute general  
89 autophagy (Jung et al., 2020) and the selective clearance of certain organelles such as  
90 peroxisomes (Young et al., 2019). However, the mutants are hypersensitive to heat, drought,  
91 oxidative, and salt stress and over-accumulate cytoplasmic protein aggregates (Zhou et al.,  
92 2013). Taken together, NBR1 appears to be required for some but not all autophagy-dependent  
93 events, consistent with a role in selective autophagy.

94 Chloroplast turnover involves multiple routes that are dependent on autophagy and/or  
95 the ubiquitin-proteasome system. Several ATG8-dependent autophagic routes control the  
96 piecemeal turnover of chloroplast components *via* Rubisco-containing bodies (Chiba et al.,  
97 2003; Ishida et al., 2008; Spitzer et al., 2015), AT11-PS (ATG8-INTERACTING PROTEIN 1)  
98 bodies (Michaeli et al., 2014), and SSLG (small starch-like granule) bodies (Wang et al., 2013)  
99 as well as the engulfment of whole photodamaged chloroplasts through microautophagy (Izumi  
100 et al., 2017). Outer envelope proteins, including components of the outer envelope translocon  
101 complex (TOC), can be ubiquitylated by chloroplast membrane-localized ubiquitin E3 ligase SP1  
102 (SUPPRESSOR OF PPI1 LOCUS 1) and extracted from the envelope membrane by the  $\beta$ -barrel  
103 channel protein SP2 and the AAA+ ATPase CDC48 for degradation by the 26S proteasome in a  
104 process named chloroplast-associated degradation (CHLORAD) (Ling et al., 2012; Ling et al.,  
105 2019). The cytosolic E3 ligase PLANT U-BOX4 (PUB4) also ubiquitylates chloroplast envelope  
106 proteins in response to oxidative stress (Woodson et al., 2015). More recently, proteins within

107 the chloroplast lumen (e.g. thylakoid and stroma proteins) were also shown to be targeted by  
108 ubiquitylation for break down *via* the proteasomes under oxidative stress (Li et al., 2022; Sun et  
109 al., 2022b). However, it remains unclear how ubiquitylation occurs inside chloroplasts.

110 Here, we show that NBR1 associates with photodamaged chloroplasts *via* its ubiquitin-  
111 binding UBA domain and mediates their vacuolar degradation by an autophagic pathway  
112 independent of ATG7, and therefore, of ATG8 lipidation. NBR1 associates with the surface and  
113 interior of chloroplasts without the need for intact translocon complexes within the outer and  
114 inner membranes. We proposed that photodamaged chloroplasts lose structural integrity of  
115 their envelopes, thus allowing access of cytosolic components such as the ubiquitylation  
116 machinery and NBR1 into the plastid interior and microautophagic clearance.

117

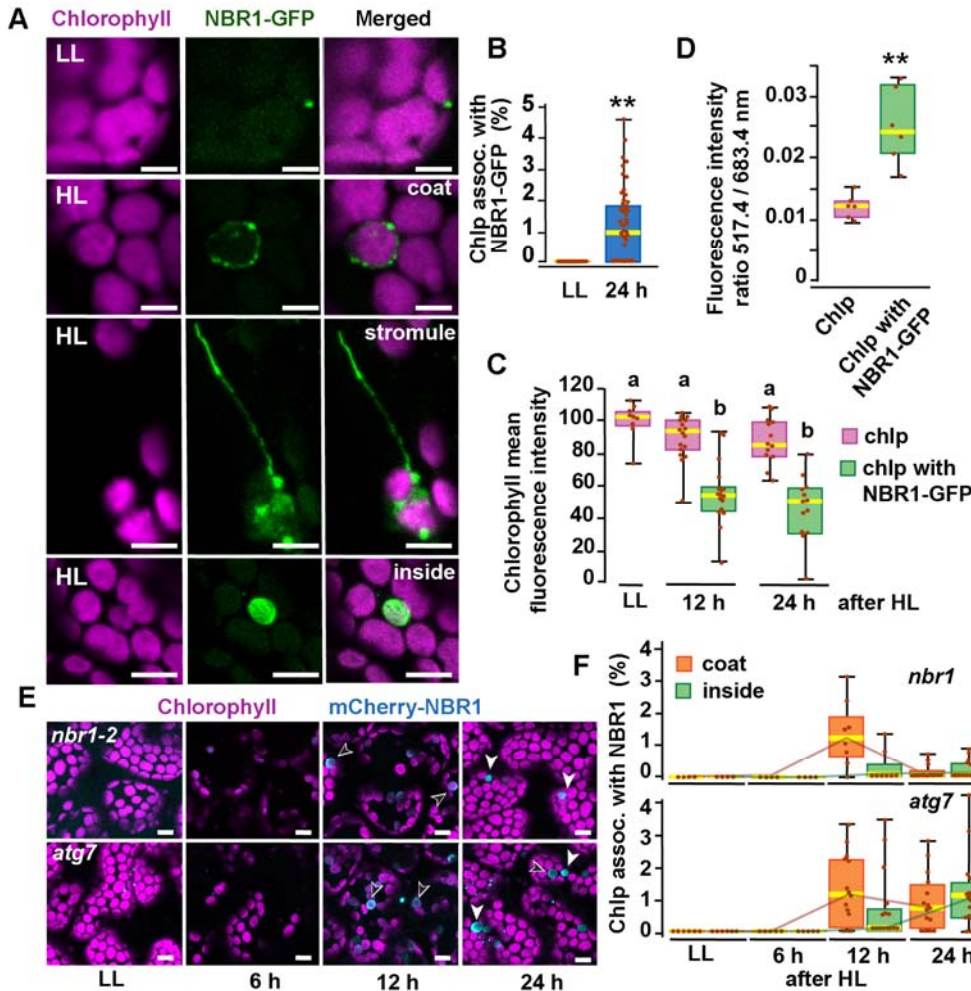
## 118 **Results**

### 119 **NBR1 associate with chloroplasts upon exposure to high light.**

120 To determine whether the autophagy receptor NBR1 is involved in chloroplast turnover upon  
121 photoradiation damage, we imaged by confocal microscopy the NBR1-GFP fusion protein  
122 expressed under the control of the NBR1 promoter (*ProNBR1:NBR1-GFP*; (Hafren et al., 2017;  
123 Thirumalaikumar et al., 2021) in seedlings grown under low light (LL; 40  $\mu\text{mol m}^{-2} \text{s}^{-1}$ ) at 22°C  
124 and exposed to high light (HL; 1500  $\mu\text{mol m}^{-2} \text{s}^{-1}$ ) at 12°C for 2 h, with a focus on the sub-  
125 adaxial epidermal mesophyll layer (mesophyll cells under the cotyledon adaxial epidermis)  
126 exposed to HL. Under LL, NBR1 was typically found in cytosolic puncta within cotyledons that  
127 likely represent aggresome condensates (Svenning et al., 2011; Jung et al., 2020) and did not  
128 colocalize with chloroplasts seen by chlorophyll autofluorescence (Fig. 1). After exposing  
129 seedlings to HL and allowing them to recover under LL for 24 h, 2% of the chloroplasts in HL-  
130 exposed mesophyll cells became heavily decorated with NBR1-GFP (Fig. 1A, B). NBR1-GFP  
131 either coated the surface of these chloroplasts or, in a few cases, localized inside (Fig. 1A).  
132 Some NBR1-GFP signal in hypocotyl cells was also associated with stromules (Fig. 1A).

133 To determine whether NBR1-GFP associated with photodamaged chloroplasts, we  
134 measured chlorophyll intrinsic fluorescence from seedlings either kept under LL or left to  
135 recover after HL exposure. In cotyledons exposed to HL, chloroplasts not labeled by NBR1-  
136 GFP had chlorophyll intensity values similar to those of control chloroplasts kept under LL. In  
137 contrast, NBR1-GFP-decorated chloroplasts showed a significant decrease in chlorophyll  
138 fluorescence intensity (Fig. 1C), consistent with chlorophyll breakdown after photodamage  
139 (Nakamura et al., 2018). As an indicator of chloroplast photodamage, we quantified the

140 chlorophyll fluorescence intensity ratio measured at 517 and 683 nm (Nakamura et al., 2018),  
 141 and found a statistically significant increase in this ratio for NBR1-GFP-decorated chloroplasts  
 142 after HL exposure (Fig. 1D).



143

144 **Figure 1. NBR1 associates with chloroplasts after HL exposure.**

145 **(A)** Confocal imaging of NBR1-GFP and chlorophyll autofluorescence in cotyledons and hypocotyl cells of  
 146 8-day old wild type seedlings grown under low light (LL,  $40 \mu\text{mol m}^{-2} \text{s}^{-1}$ ) or left to recover for 24 h after  
 147 exposure to 2 h HL conditions (HL,  $1,500 \mu\text{mol m}^{-2} \text{s}^{-1}$ ) at  $12^\circ\text{C}$ . After HL exposure, NBR1 either coated  
 148 the surface of chloroplasts and stromules or localized inside chloroplasts.

149 **(B)** Box and whisker plots represent the percentage of chloroplast associated with NBR1-GFP in 8-day  
 150 old seedlings grown under LL or 24 h after HL exposure. At least 35 confocal images from 7-12  
 151 cotyledons were analyzed for each condition.

152 **(C)** Box and whisker plots showing chlorophyll mean intensity from chloroplast with and without NBR1-  
 153 GFP in cotyledons from 8-day old seedling grown under LL or exposed to HL and left to recover for 12 h

154 or 24 h. Representative experiment showing data from at least 5 randomly selected chloroplasts for each  
155 condition.

156 **(D)** Ratio of chlorophyll fluorescence intensities at 517.4 m and 683.4 nm. Representative experiment  
157 showing data from 6 chloroplasts with or without NBR1-GFP from 8-day old cotyledons 24 h after HL  
158 exposure. Different letters on the graph indicate significant difference ( $p < 0.05$ ) calculated by one-way  
159 ANOVA followed by Tukey's test.

160 **(E)** Confocal imaging of cotyledons from 8-day old seedling expressing mCherry-NBR1 in *nbr1* and *atg7*  
161 plants grown under LL or exposed to HL and left to recover for 6, 12, and 24 h. Hollow arrowheads and  
162 filled arrowheads indicate the mCherry-NBR1 coats and inside chloroplasts, respectively.

163 **(F)** Box and whisker plots showing the percentage of chloroplasts associated with mCherry-NBR1 as  
164 coats (orange) or inside chloroplasts (green) under LL, and at the indicated recovery times after HL  
165 exposure. The top and bottom plots show measurements from *nbr1* and *atg7*, respectively.  
166 Representative experiment analyzing between 4 and 15 fields from 3-6 cotyledons for each condition and  
167 genotype.

168 Box and whisker plots in B, C, D, and F display the variation in data through quartiles; the middle line  
169 indicates the median and whiskers show the upper and lower fences. Asterisks in B and D denote  
170 significant differences based on t-tests (\*\*,  $p < 0.01$ ).

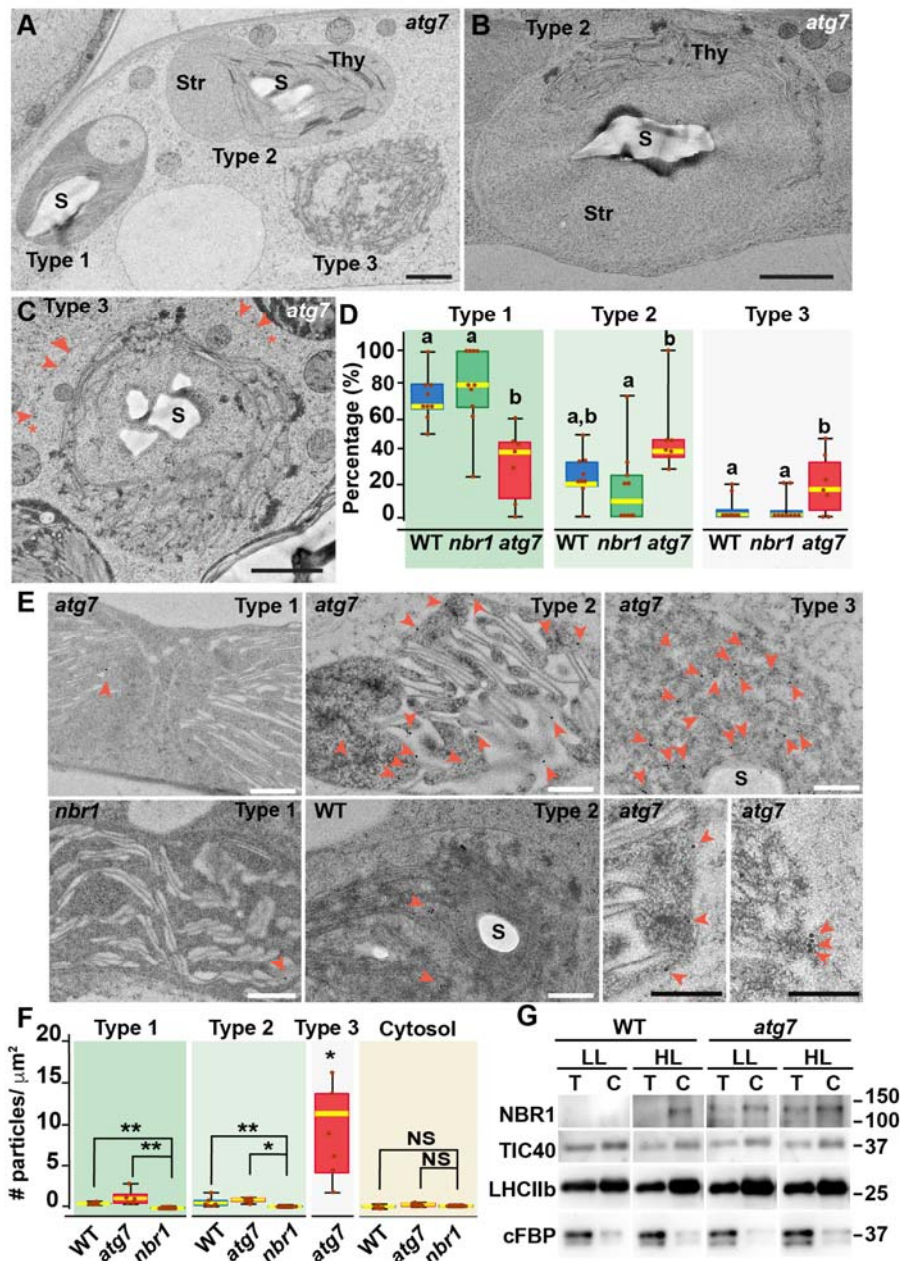
171 Scale bars = 5  $\mu$ m in A and E.

172

173 Previous studies showed that the recruitment of ATG8 to chloroplasts after HL exposure  
174 depends on the canonical ATG machinery (Nakamura et al., 2018). Consequently, we tested  
175 whether this was also the case for NBR1 by analyzing seedlings expressing mCherry-NBR1  
176 under the control of the *UB10* promoter in the *nbr1-2* (*nbr1*; Zhou et al., 2013; Jung et al., 2020)  
177 and *atg7-2* (*atg7*; Chung et al., 2010) mutant backgrounds. Upon HL exposure, we detected by  
178 confocal microscopy mCherry-NBR1 associated with chloroplasts in both *nbr1* and *atg7*  
179 cotyledon mesophyll cells (Fig. 1E, F). In both genotypes, the mCherry-NBR1 signal coated the  
180 chloroplast surface (open arrows in Fig. 1E) as well as its interior (solid arrows in Fig. 1E),  
181 indicating that ATG7, and by inference ATG8 lipidation, are not required for recruiting NBR1 to  
182 chloroplasts upon HL exposure.

183 To confirm that NBR1 was indeed internalized into chloroplasts, we examined the  
184 ultrastructural features of chloroplasts under HL conditions by transmission electron microscopy  
185 and localized NBR1 with anti-NBR1 antibodies. First, we analyzed the structural alterations of  
186 chloroplasts after 24 h exposure to HL in wild-type, *atg7*, and *nbr1* cotyledons processed by  
187 high-pressure frozen/freeze substitution. Based on the degree of structural integrity, we found  
188 three morphologically distinct chloroplast types often in the same cell although with different

189 frequencies. Type-1 chloroplasts had normal thylakoids and electron-dense stroma; Type-2  
 190 chloroplasts had dilated and lighter stroma with thylakoid membranes partially disorganized and  
 191 displaced to one side of the chloroplast; and Type-3 chloroplasts contained highly disorganized  
 192 thylakoids, light stroma, and clear signs of chloroplast envelope rupture (Fig. 2A-C).



193  
 194 **Figure 2. Ultrastructure of chloroplasts in wild-type, *atg7*, and *nbr1* cotyledons 24 h after HL**  
 195 **exposure.**

196 (A) Transmission electron micrograph of a high-pressure frozen/freeze-substituted *atg7* cotyledon  
 197 mesophyll cell from 8-day old seedlings exposed to HL and left to recover for 24 h. Three different types



198 of chloroplasts based on their structural integrity are seen. Type-1 chloroplasts with electron dense  
199 stroma and tightly appressed thylakoids, Type-2 chloroplasts with lighter stroma and partially  
200 disorganized thylakoids, and Type-3 chloroplasts with ruptured envelopes, disorganized thylakoid  
201 membranes and a stroma region with similar electron density and appearance to the cytoplasm.  
202 **(B, C)** Representative Type-2 **(B)** and Type-3 **(C)** chloroplasts in an *atg7* mesophyll cells. Note in (C) that  
203 the outer and inner envelopes (arrowheads) are disrupted in several sites (asterisks) exposing the interior  
204 of the chloroplast, including thylakoid membranes to the cytosol.  
205 **(D)** Box and whisker plots showing the percentage of Type-1, -2, and -3 chloroplasts per mesophyll cell  
206 section in wild-type Col-0 (WT), *nbr1*, and *atg7* cotyledons. Different letters on the graph indicate  
207 significant difference ( $p < 0.05$ ) calculated by one-way ANOVA followed by Tukey's test.  
208 **(E)** Immunogold labeling with anti NBR1 antibodies on chloroplasts of WT, *nbr1*, and *atg7* mutant  
209 mesophyll cells exposed to HL followed by 24 h recovery. Red arrowheads indicate gold particles on  
210 chloroplasts.  
211 **(F)** Quantification of anti-NBR1 gold labeling on Type-1, -2, and -3 chloroplasts and cytoplasm from WT,  
212 *atg7*, and *nbr1* mutant mesophyll cells exposed to HL. A t-test was used to compare values between  
213 mutant and WT samples; \* and \*\* indicate  $p < 0.05$  and  $p < 0.01$ , respectively.  
214 **(G)** Immunoblot detection of NBR1, TIC40 (chloroplast inner envelope protein), LHCIIB (thylakoid protein),  
215 and cFBP (cytosolic protein) in total protein extracts (T) and chloroplast protein fraction (C) from 4-week-  
216 old WT and *atg7* plants grown under LL or exposed to HL and let recover for 24h.  
217 Box and whisker plots in D and F show the variation in data through quartiles; the middle line indicates  
218 the median and whiskers show the upper and lower fences.  
219 S, starch; St, stroma; Thy, thylakoids. Scale bars: 1  $\mu\text{m}$  in A, B, C; 500 nm in E.

220

221 Type-3 chloroplasts were significantly more abundant in the *atg7* cotyledons, whereas  
222 their frequency in *nbr1* cotyledons was indistinguishable from that in wild-type cotyledons (Fig.  
223 2D). Using anti-NBR1 antibodies (Figure 2-figure supplement 1), we performed immunogold  
224 labeling to detect the native NBR1 protein in the three types of chloroplasts from wild-type and  
225 *atg7* cotyledons exposed to HL, in this case using *nbr1* seedlings grown under similar conditions  
226 as a negative control (Fig. 2E, F). Whereas we did not detect labeling of NBR1 in the cytosol,  
227 all chloroplasts in wild-type and *atg7* seedlings exposed to HL showed significantly higher  
228 labeling than those seen in the *nbr1* cotyledons (Fig. 2E, F).

229 Corroborating the NBR1-GFP and mCherry-NBR1 confocal imaging results, endogenous  
230 NBR1 was detected on the surface and inside wild-type and *atg7* chloroplasts (Fig. 2E). Among  
231 the three types of chloroplasts, Type-3 chloroplasts, which were most abundant in *atg7*  
232 cotyledons (Fig. 2D), showed the heaviest internal labeling, both on thylakoids and on the

233 stroma (Fig. 2F). As Type-3 chloroplasts showed disorganized thylakoids, this labeling is  
234 consistent with the preferential recruitment of NBR1-GFP to damaged chloroplasts as judged by  
235 their decreased levels of chlorophyll autofluorescence (Fig. 1C).

236 To further corroborate the association of NBR1 with photodamaged chloroplasts, we  
237 isolated chloroplasts from 4-week-old wild-type and *atg7* mutant plants kept under LL or  
238 exposed to HL conditions and allowed to recover for 24 h (Fig. 2G). We assessed the purity of  
239 our chloroplast fraction by testing the enrichment of chloroplast proteins such as TIC40 (inner  
240 envelope) and anti-LHCIIb (thylakoid), and the depletion of the cytosolic fructose  
241 biphosphatase (FBPase). NBR1 was barely detectable in either the total extract or the  
242 chloroplast fraction from wild-type plants kept under LL (Fig. 2G). However, after HL exposure,  
243 NBR1 became much more abundant in the chloroplast fraction. Similarly, the association of  
244 NBR1 with chloroplasts under HL was also apparent in *atg7* seedlings (Fig. 2G), further  
245 confirming that ATG7 is not required for recruiting NBR1 to photodamaged chloroplasts.

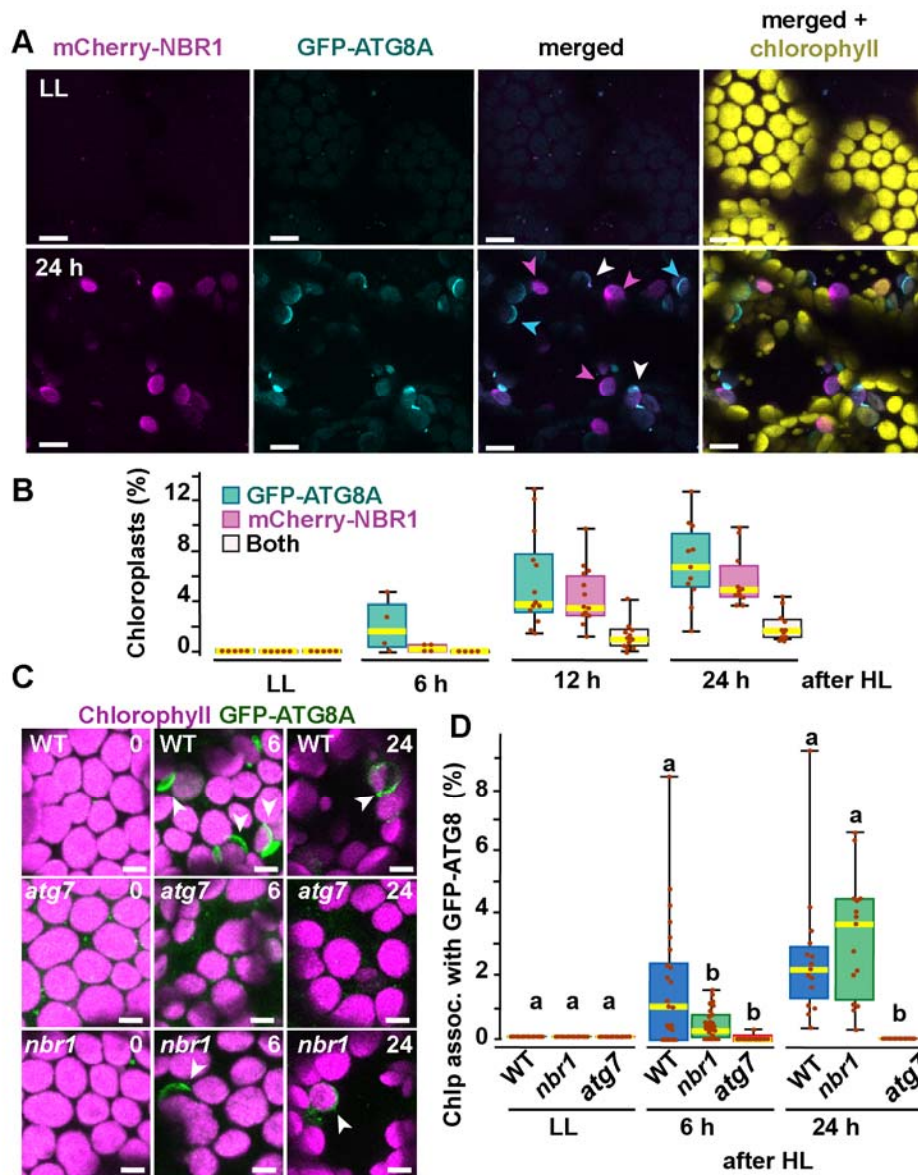
246

#### 247 **ATG8 and NBR1 are recruited to different populations of damaged chloroplasts.**

248 ATG8 was previously reported to coat photodamaged chloroplasts in *Arabidopsis* (Nakamura et  
249 al., 2018). Since NBR1 interacts with ATG8, we tested whether NBR1 and ATG8 were recruited  
250 to the same chloroplast population. We used seedlings expressing both mCherry-NBR1 and  
251 GFP-ATG8, exposed them to HL, and then imaged them during a 24 h recovery window (Fig.  
252 3A, B). As expected, neither mCherry-NBR1 or GFP-ATG8 associated with chloroplasts under  
253 LL conditions. However, after the HL treatment, the chloroplast association of both proteins  
254 became evident at 6 h during recovery. By 12 h after HL exposure, approximately 4% and 5%  
255 of the total mesophyll chloroplasts were decorated by either mCherry-NBR1 or GFP-ATG8,  
256 respectively, but only 1% of chloroplasts were decorated with both (Fig. 3A, B). A similar trend  
257 was observed 24 h after HL exposure; approximately 7% of the chloroplasts were labeled with  
258 GFP-ATG8, 5.5% were labeled with mCherry-NBR1 but only 2% of the chloroplasts were  
259 associated with both (Fig 3A, B). This dichotomy suggests that NBR1 and ATG8 are recruited  
260 to unique populations of chloroplasts, consistent with their distinct dependence on the ATG  
261 machinery for chloroplast recruitment.

262 To further assess a functional disconnection between ATG8 and NBR1 in the  
263 degradation of photodamaged chloroplasts, we imaged GFP-ATG8A in *nbr1*, *atg7*, and wild-  
264 type seedlings exposed to HL (Fig. 3C, D). As previously reported (Nakamura et al., 2018),

265 GFP-ATG8 failed to label photodamaged chloroplasts in *atg7* cotyledons. Compared to wild  
 266 type, we detected a significant decrease in the proportion of chloroplasts decorated by GFP-  
 267 ATG8A in the *nbr1* mutant at 6 h during recovery from HL exposure; however, by 24 h, similar  
 268 proportions of both wild type and *nbr1* chloroplasts were coated by GFP-ATG8A (Fig. 3C, D).  
 269 Taken together, these results show that NBR1 and ATG8A are recruited to different populations  
 270 of photodamaged chloroplasts and that NBR1 is only partially required for the early association  
 271 of GFP-ATG8A with these organelles.



272

273 **Figure 3. Recruitment of NBR1 and ATG8A to photodamaged chloroplasts.**

274 **(A)** Confocal imaging of cotyledon mesophyll cells from 8-day old seedlings expressing mCherry-NBR1  
275 and GFP-ATG8A under LL (top) and at 24 h after HL exposure (bottom). Magenta, cyan, and white  
276 arrowheads indicate chloroplasts associated with mCherry-NBR1, GFP-ATG8, or both, respectively.

277 **(B)** Box and whisker plots showing the percentage of chloroplasts associated with GFP-ATG8A (cyan),  
278 mCherry-NBR1 (magenta), or both (white) under LL and during recovery after HL exposure.

279 **(C)** Confocal imaging of GFP-ATG8A in cotyledons of 8-day old wild-type Col-0 (WT), *atg7*, and *nbr1*  
280 seedlings grown under LL, and 6 and 24 h after HL treatment. Arrowheads indicate chloroplasts  
281 associated with GFP-ATG8A.

282 **(D)** Box and whisker plot displaying the percentage of chloroplast associated with GFP-ATG8A in  
283 different genotypes, under LL and recovery after HL. Different letters on the graph indicate significant  
284 difference ( $P < 0.05$ ) calculated by one-way ANOVA followed by Tukey's test.

285 Box and whisker plots in B and D show the variation in data through quartiles; the middle line indicates  
286 the median and whiskers show the upper and lower fences.

287 Scale bars: 10  $\mu\text{m}$  in A and C.

288

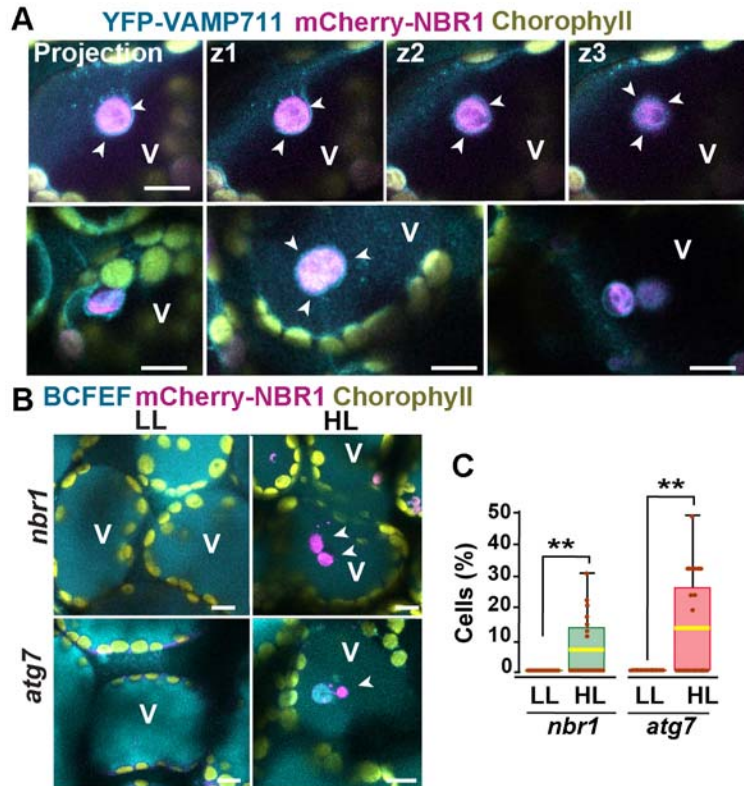
### 289 **NBR1-decorated chloroplasts are delivered to vacuoles in an ATG7-independent manner.**

290 Previous studies have shown that ATG8-associated chloroplasts are delivered to vacuoles  
291 through a microautophagic process that relies on the canonical ATG machinery (Izumi et al.,  
292 2017; Nakamura et al., 2018). To determine whether this is also the case for NBR1-decorated  
293 chloroplasts, we co-expressed mCherry-NBR1 with the tonoplast marker YFP-VAMP711  
294 (Geldner et al., 2009) in *nbr1* seedlings. After HL exposure, mCherry-NBR1-positive  
295 chloroplasts associated with deep tonoplast invaginations (Fig. 4A), which led to their vacuolar  
296 internalization by microautophagy, in a process topologically similar to that previously described  
297 for ATG8-decorated chloroplasts (Izumi et al., 2017). Similarly, we were able to detect NBR1-  
298 positive chloroplasts inside vacuoles of the mCherry-NBR1 seedlings stained with the vacuolar  
299 dye BCECF (Scheuring et al., 2015) 24 h after HL exposure (Fig. 4B, C). Surprisingly, NBR1-  
300 decorated chloroplasts were also seen inside vacuoles of *atg7* seedlings (Fig. 4B, C).

301 Taken together, these results are consistent with NBR1 associating with chloroplasts  
302 targeted for vacuolar degradation through ATG7-independent microautophagy. In addition, the  
303 higher number of NBR1-positive photodamaged chloroplasts in *atg7* seedlings (Fig. 2) does not  
304 seem to arise from a failure to deliver these chloroplasts to the vacuole but more likely to the  
305 higher accumulation of photodamaged chloroplasts in the *atg7* mutant.

306

307



308

309 **Figure 4: Vacuolar delivery of NBR1-positive chloroplast into the vacuole.**

310 **(A)** Projection of three confocal images (z1-z3) and several other confocal images of cotyledon mesophyll  
311 cells from 1-week-old, wild-type seedlings expressing the tonoplast marker YFP-VAMP711 and mCherry-  
312 NBR1, 24 h after HL exposure. Chloroplast labeled by mCherry-NBR1 were surrounded by the tonoplast  
313 (arrowheads) and internalized into the vacuole (V) through microautophagy.

314 **(B)** Confocal images of *nbr1* and *atg7* cotyledon mesophyll cells at 24 h after HL exposure and stained  
315 with the vacuolar dye BCECF. Note the mCherry-NBR1-labeled chloroplasts inside the vacuoles.

316 **(C)** Box and whisker plot displaying the percentage of cells containing mCherry-NBR1-labeled  
317 chloroplasts inside their vacuoles. Boxes show the variation in data through quartiles; the middle line  
318 indicates the median and whiskers show the upper and lower fences.

319 A t-test was used to compare values between LL and recovery after HL \*\* indicate  $p < 0.01$ .

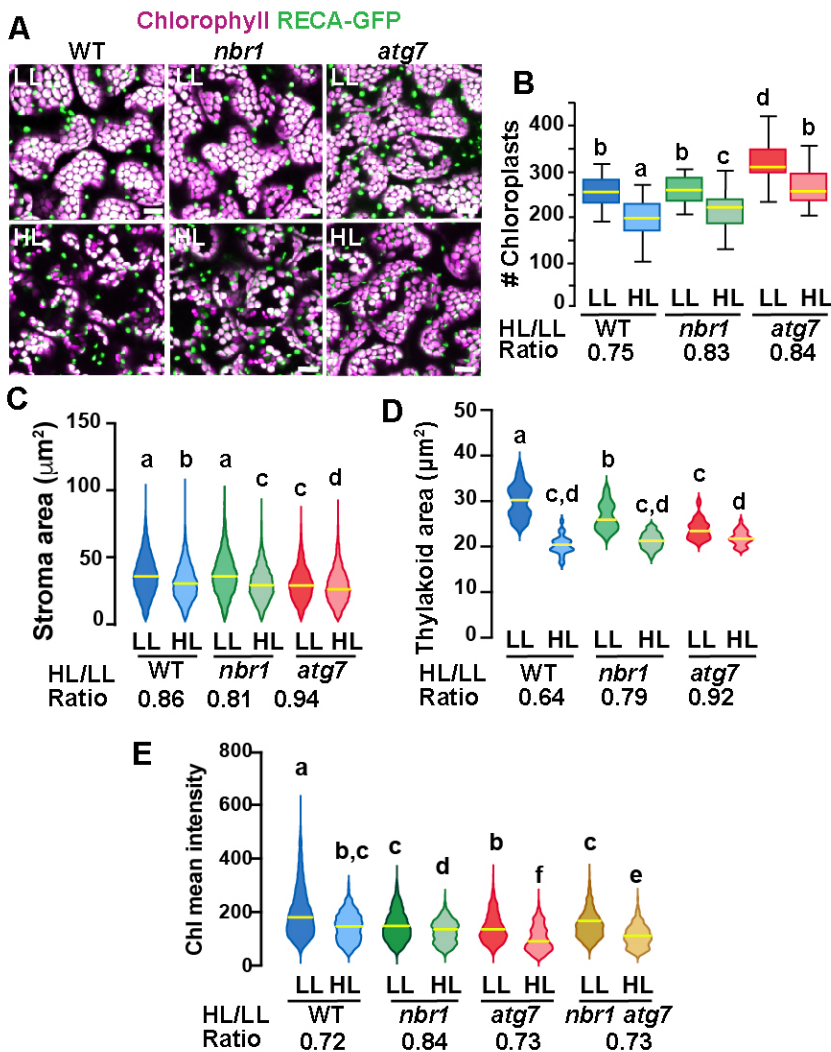
320 Scale bars: 10  $\mu$ m in A and B.

321

322 **Impaired remodeling of chloroplasts in *atg7* and *nbr1* mutants.**

323 If NBR1 is critical for targeting photodamaged chloroplasts to the vacuole, we reasoned that  
324 *nbr1* mutations would reduce the loss of chloroplasts after HL, as it has been shown for the *atg5*  
325 and *atg7* mutants (Izumi et al., 2017). To test this scenario, we expressed RECA-GFP, a

326 stromal marker bearing the transit peptide of Arabidopsis RECA fused to GFP (Kohler et al.,  
 327 1997; Spitzer et al., 2015), and imaged the cotyledon sub-axial epidermal mesophyll layer  
 328 from 8-day-old seedlings by confocal microscopy. We found that, under LL conditions *atg7* but  
 329 not *nbr1* mutant seedlings had a higher density of chloroplasts compared to wild type (Fig. 5A,  
 330 B). Twenty four hours after HL, there was a reduction in chloroplast density in all three  
 331 genotypes but the decrease was less pronounced in *atg7* and *nbr1* (17% and 16% reduction,  
 332 respectively) compared to the wild-type control (25% reduction; Fig. 5A, B), consistent with  
 333 impaired turnover of chloroplasts in both *atg7* and *nbr1* mutants.



334

335 **Figure 5. Chloroplast remodeling after HL exposure.**

336 (A) Projections of 20 confocal images along a z-stack taken from the adaxial side of cotyledon mesophyll  
 337 cells from 8-day old wild-type (WT), *atg7*, and *nbr1* seedlings expressing RECA-GFP. Seedlings were  
 338 grown under LL, exposed to HL for 2 h and let recover for 24 h.

339 **(B)** Chloroplast density in adaxial-facing mesophyll cells (number of chloroplasts per  $2.16 \mu\text{m}^2$ ) based on  
340 confocal images. At least 20 randomly selected areas from 6-9 cotyledons were considered in this  
341 analysis. Boxes show the variation in data through quartiles; the middle line indicates the median and  
342 whiskers show the upper and lower fences.

343 **(C)** Stroma area ( $\mu\text{m}^2$ ) as measured by the RECA-GFP fluorescence signal per individual chloroplast  
344 imaged by confocal microscopy. Lines in violin plots indicate median values. At least 25 individual  
345 chloroplasts were measured for each genotype and condition.

346 **(D)** Thylakoid area ( $\mu\text{m}^2$ ) as measured by chlorophyll fluorescence signal area per individual chloroplast.  
347 Line in violin plots indicate median values. At least 5,000 individual chloroplasts were measured for each  
348 genotype and condition.

349 **(E)** Chlorophyll mean intensities measured in individual chloroplasts by multiphoton imaging. Between  
350 1,300 and 2,600 individual chloroplasts were measured for each genotype and condition. Lines in violin  
351 plot indicate median values.

352 In B to E, the HL/LL ratio was calculated by dividing the average value from HL-treated plants by the  
353 average value of the plants grown under LL. Different letters denote significant differences from each  
354 other based on two-way ANOVA followed by Tukey's test ( $p < 0.05$ ).

355 Scale bars:  $10 \mu\text{m}$  in A.

356

357 To examine whether chloroplast size also changed upon HL exposure, we measured the  
358 area of both RECA-GFP signal (stroma) and chlorophyll autofluorescence (thylakoids) in  
359 individual chloroplasts. Overall, there was a decrease in both RECA-GFP and chlorophyll area  
360 of individual chloroplasts 24 h after HL exposure in the three genotypes. However, whereas the  
361 *nbr1* and wild type RECA-GFP-decorated chloroplasts were similar in size under LL, the  
362 decrease in RECA-GFP area upon HL treatment was slightly more abrupt in *nbr1* (19%  
363 reduction) than in control cotyledons (14% reduction; Fig. 5A, C). RECA-GFP-decorated *atg7*  
364 chloroplasts were smaller than those in control and *nbr1* cotyledons and showed a small (6%)  
365 reduction in area upon HL treatment (Fig. 5A, C). Chlorophyll areas were smaller in *nbr1* and  
366 *atg7* chloroplasts compared to the wild-type control even under LL conditions, and underwent  
367 an attenuated reduction after HL exposure (21% and 18% in *nbr1* and *atg7*, respectively),  
368 compared to control chloroplasts (36% reduction; Fig. 5A, D). Taken together, these results  
369 demonstrate that although both *atg7* and *nbr1* retained more chloroplasts than control plants  
370 after HL exposure (Fig 4E), the remaining chloroplasts in the mutants were smaller, both in  
371 stroma and thylakoid areas.

372 These unique chloroplast dynamics in *nbr1*, *atg7*, and wild-type plants suggested that  
373 although ATG7 and NBR1 are both important for chloroplast turnover, they control different

374 aspects of chloroplast remodeling/turnover after HL radiation. To further understand how  
375 chloroplasts are differentially affected, we used multiphoton imaging to excite and measure  
376 chlorophyll mean intensities under LL and 24 h after HL exposure in *nbr1* and *atg7* seedlings,  
377 together with a previously characterized *nbr1-2 atg7-2* double mutant (*nbr1 atg7*; Jung et al.,  
378 2020). Compared to controls, mean chlorophyll fluorescence intensity in all three mutants was  
379 weaker than wild type under LL conditions. This intensity decreased approximately 27-28% in  
380 wild type and the *atg7* mutant after HL (based on ratio of chlorophyll mean intensities between  
381 HL and LL values), but only 16% in the *nbr1* mutant (Fig. 5E). Unexpectedly, the mean  
382 chlorophyll intensity values from *nbr1 atg7* mutant under LL and after HL treatment were  
383 intermediates between those from the single *nbr1* and *atg7* mutant seedlings. These results  
384 indicate that mutations in both *NBR1* and *ATG7* affect either chlorophyll abundance and/or  
385 chlorophyll photochemical properties even under LL conditions.

386  
387 **Proteome profiling supports NBR1- and ATG7-dependent pathways for clearing**  
388 **photodamaged chloroplasts.**

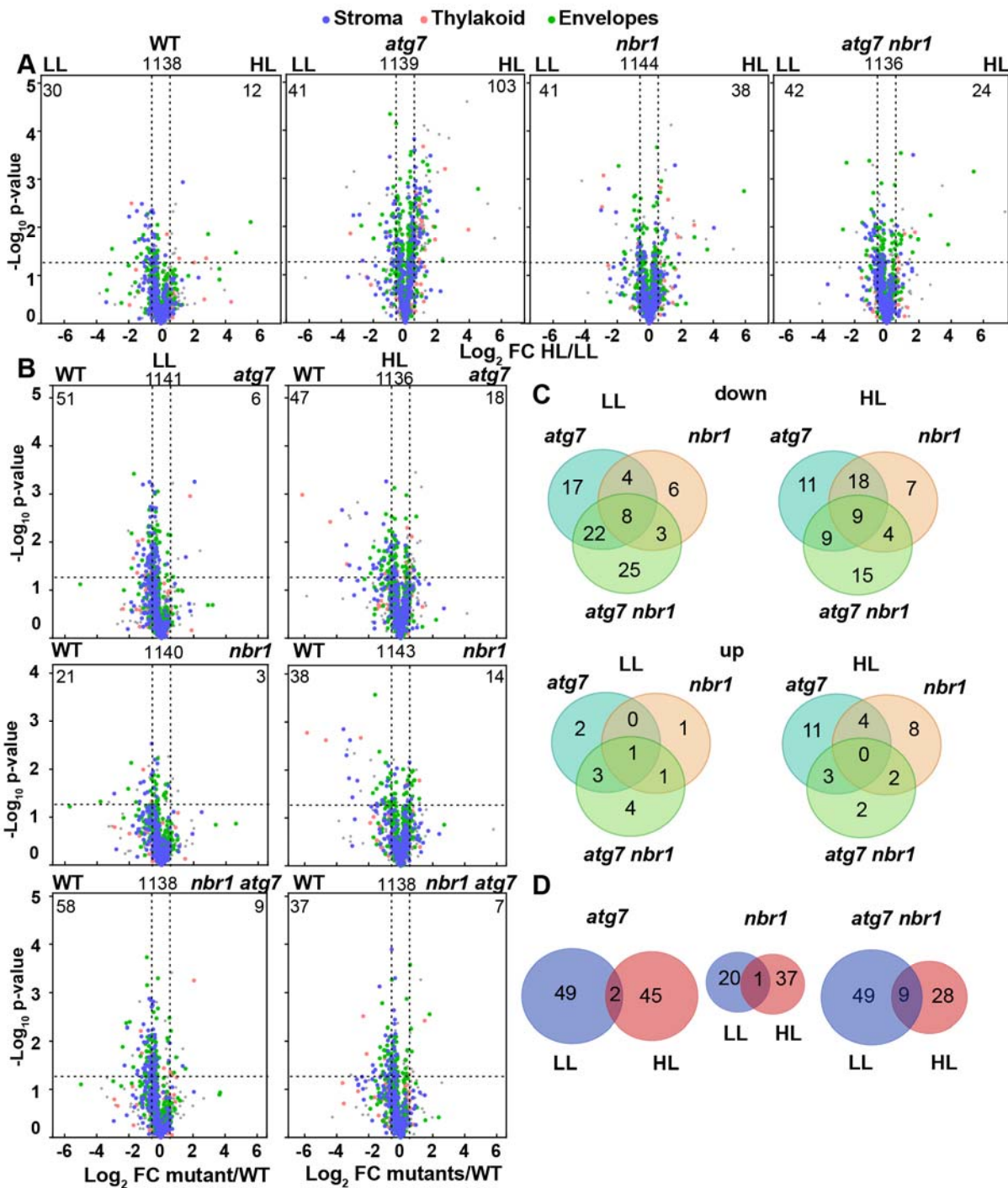
389 To further understand the function of *NBR1* and *ATG7* in chloroplast remodeling and turnover,  
390 we analyzed by mass spectrometry (MS) the total proteome of 1-week-old *atg7*, *nbr1*, *nbr1 atg7*  
391 double mutant, and wild-type seedlings grown under LL and at 24 h after HL treatment (Fig. 6,  
392 Fig. 6-figure supplements 1 and 2, Suppl. Tables 1-3).

393 HL treatment induced a relatively mild changes in the total proteome of all four  
394 genotypes. We identified 164 differentially accumulated proteins (DAPs) after HL treatment as  
395 compared to LL (4.5% of the 3682 total detected proteins; 55 more and 109 less abundant) in  
396 wild type; 622 DAPs in *atg7* (17% of the 3693 total detected proteins; 444 more and 178 less  
397 abundant); 313 DAPs in *nbr1* (8.5% of the 3683 total detected proteins; 166 more and 147 less  
398 abundant); and 215 DAPs in the *nbr1 atg7* double mutant (6% of the 3668 total detected  
399 proteins; 102 more and 113 less abundant) (Fig. 6-figure supplement 2 and Suppl. Tables 4-7).  
400 Compared to wild-type seedlings, the three analyzed mutants showed differences in their  
401 proteome profiles under both LL and HL conditions (Fig. 6-figure supplement 2, Suppl. Tables 8-  
402 13); under HL and compared to WT, we detected 456 DAPs in *atg7* (166 less and 290 more  
403 abundant), 251 DAPs in *nbr1* (170 less and 81 more abundant), and 266 DAP in *nbr1 atg7* (95  
404 less and 171 more abundant) (Fig. 6-figure supplement 2, Suppl. Tables 8-10), showing a  
405 general trend of steady-state protein levels increasing in *atg7* and *nbr1 atg7* and decreased  
406 protein abundance in *nbr1* mutant seedlings.



407 In terms of the chloroplast proteome, all genotypes showed changes in protein  
408 abundance after HL treatment (Fig. 6A), with an over-representation of less abundant  
409 chloroplast proteins in the three mutants as compared to wild type, under both LL and after HL  
410 treatment (Fig. 6A, B). This group of less abundant proteins in the three mutants localized to  
411 stroma, thylakoids, and envelopes (Fig. 6B). Whereas the proportion of less abundant  
412 chloroplast proteins in *atg7* compared to wild type remained constant under LL and HL (4% in  
413 both cases), the proportion of less abundant proteins in *nbr1* were 1.8% and 3.3% of the  
414 identified chloroplast proteins under LL and HL, respectively. The *nbr1 atg7* mutant showed the  
415 opposite trend with fewer less abundant chloroplast proteins after HL (3%) than under LL (5%).  
416 Under HL, *atg7* showed a relative increase of approximately 20% in the proportion of less  
417 abundant chloroplast proteins compared to the *nbr1* and *nbr1 atg7* mutants (Fig. 6B).  
418 Interestingly, only 34-35% of the less abundant chloroplast proteins in *atg7* were also less  
419 abundant in *nbr1*, whereas 65-70% of the less abundant chloroplast proteins in *nbr1* showed  
420 reduced abundance in *atg7*, under both LL and HL conditions (Fig. 6C), further supporting that  
421 ATG7 and NBR1 control different aspects of chloroplast remodeling/turnover after HL.  
422 Remarkably, there was only a small overlap between the less abundant proteins in each mutant  
423 under LL and after HL treatment (Fig. 6D), suggesting that although chloroplast proteins are  
424 less abundant in the mutants under both light treatments, HL exposure triggered changes in the  
425 abundance of different sets of chloroplast proteins compared to LL conditions.

426 The observed relative decrease in chloroplast protein abundance in the three mutants  
427 was not a general trend for all organelles as might be expected if general autophagy was  
428 compromised. For example, the abundance of peroxisomal proteins were largely unchanged in  
429 *nbr1* but greater in *atg7* under HL compared to wild type (Fig. 6-figure supplement 2), consistent  
430 with a failure of the mutant to degrade damaged peroxisomes after HL exposure as previously  
431 reported in *atg7* plants (Oikawa et al., 2022).



432

433 **Figure 6. Chloroplast proteome analysis by liquid chromatography-tandem mass spectrometry**  
 434 **(LC-MS/MS).**

435 **(A)** Volcano plots showing the relative changes in chloroplast protein abundance in wild-type Col-0 (WT),  
 436 *nbr1*, *atg7*, and *nbr1 atg7* seedlings grown either under LL or exposed to HL and let recover for 24 h.  
 437 Proteins were identified by LC-MS/MS, and their average abundances calculated from the MS1 precursor  
 438 ion intensities. Only proteins with at least two peptide spectral matches were considered in this analysis.

439 Each protein is plotted based on its  $\text{Log}_2$  FC ( $>\text{Log}_2$  0.6 or  $<\text{Log}_2$  -0.6) in abundance (HL/LL) and its  $-\log_{10}$   
440  $p$ -value ( $>-\log_{10}$  1.3) in significance based on the three biological replicates.

441 **(B)** Volcano plots showing the changes in the relative abundance of chloroplast proteins in mutants  
442 compared to wild type WT, under two different light conditions.

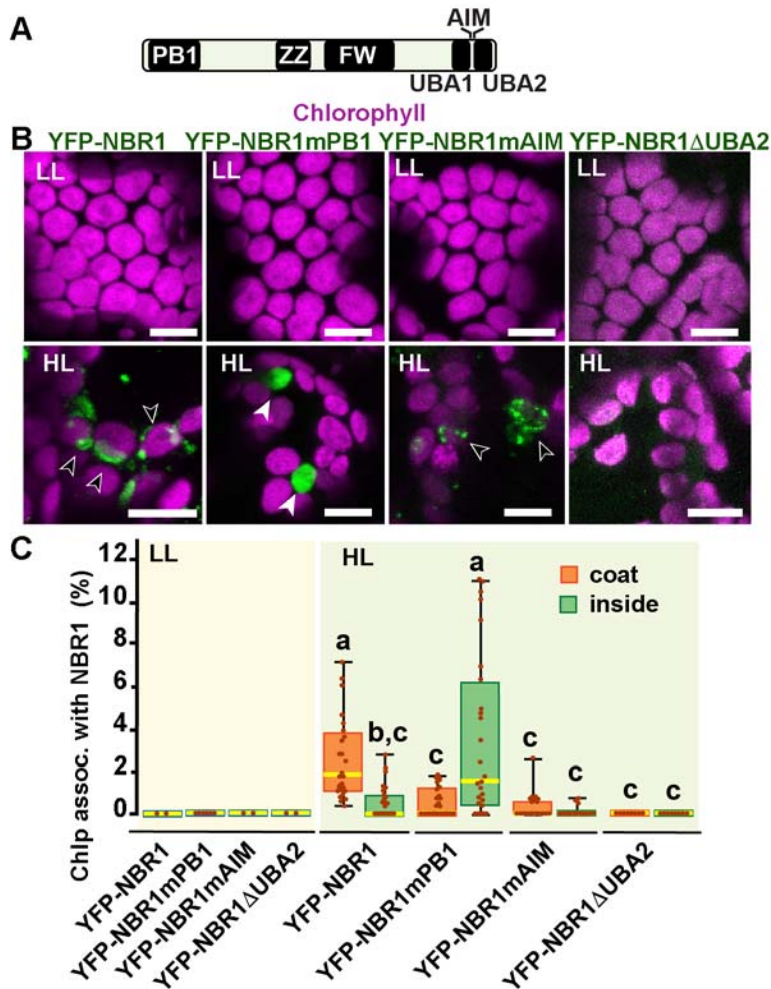
443 **(C)** Venn's diagrams depicting the overlap among chloroplast DAPs (either less or more abundant) in  
444 mutants compared to WT, either under LL or after HL exposure.

445 **(D)** Overlap of less abundant chloroplast proteins in *atg7*, *nbr1*, and *nbr1 atg7* compared to WT, either  
446 under LL or after HL exposure.

447

#### 448 **Contributions of NBR1 domains to chloroplast recruitment.**

449 To identify the NBR1 domains that help NBR1 associate with photodamaged chloroplasts, we  
450 expressed in the *nbr1-1 background* several mutant versions of YFP-NBR1 missing key domain  
451 functions, such as NBR1-mPB1 with a point mutation (K11A) in the PB1 domain (Fig. 7A, B)  
452 that disrupts NBR1 oligomerization (Hafren et al., 2017), NBR1-mAIM with two point mutations  
453 in the AIM domain (W661A, I664A) that block interaction with ATG8 (Svenning et al., 2011;  
454 Hafren et al., 2017), and NBR1- $\Delta$ UBA2 missing the UBA2 domain (Fig. 7A, B) and therefore,  
455 unable to bind ubiquitin (Svenning et al., 2011; Hafren et al., 2018). All fluorescent NBR1 fusion  
456 proteins remained cytosolic under LL condition (Fig. 7B, C). After HL exposure, YFP-NBR1  
457 associated with photodamaged chloroplasts as expected, either forming coats (average ~3% of  
458 chloroplasts;  $n = 28$  fields) or localizing inside a small fraction of chloroplasts (average ~0.5% of  
459 chloroplasts;  $n = 28$  fields) (Fig 7B, C). YFP-NBR1mPB also localized to photodamaged  
460 chloroplasts but almost exclusively to their interior (Fig. 7B, C). Thus, although the total  
461 percentages of chloroplasts labeled by YFP-NBR1 and YFP-NBR1mPB were similar (Fig 7C),  
462 YFP-NBR1 mainly coated the surface of chloroplasts whereas most of YFP-NBR1mPB was  
463 located to the chloroplast lumen. Just like YFP-NBR1, YFP-NBR1mAIM was mostly detected  
464 as chloroplast coats (Fig. 7B and C). Interestingly, YFP-NBR1 $\Delta$ UBA2 failed to associate with  
465 chloroplasts after HL exposure (Fig. 7B, C). The expression of the same set of NBR1 mutated  
466 proteins resulted in a similar pattern of chloroplast association in the *atg7 nbr1* seedlings  
467 exposed to HL (Fig. 7-figure supplement 1). Thus, these results suggest the UBA2 domain is  
468 required for NBR1 chloroplast association whereas the PB1 domain negatively regulates NBR1  
469 intra-chloroplast localization and/or promotes degradation of NBR1-filled chloroplasts.



470

471 **Figure 7. NBR1 domains have distinct roles in recruiting NBR1 to chloroplasts after HL treatment.**

472 **(A)** Diagram of the Arabidopsis NBR1 protein and its domains. FW, Four-Tryptophan domain; PB1, Phox  
 473 and Bem1p domain; ZZ, ZZ-type zinc finger domain; UBA1 and UBA2, ubiquitin-associated domains;  
 474 AIM, ATG8-interacting motif.

475 **(B)** Confocal imaging of NBR1 mutated proteins fused to YFP expressed in 8-day-old *nbr1* seedlings  
 476 grown under LL (top) or at 24 h after HL exposure (bottom). Hollow arrowheads and filled arrowheads  
 477 indicate YFP-NBR1 coating chloroplasts and inside chloroplasts, respectively.

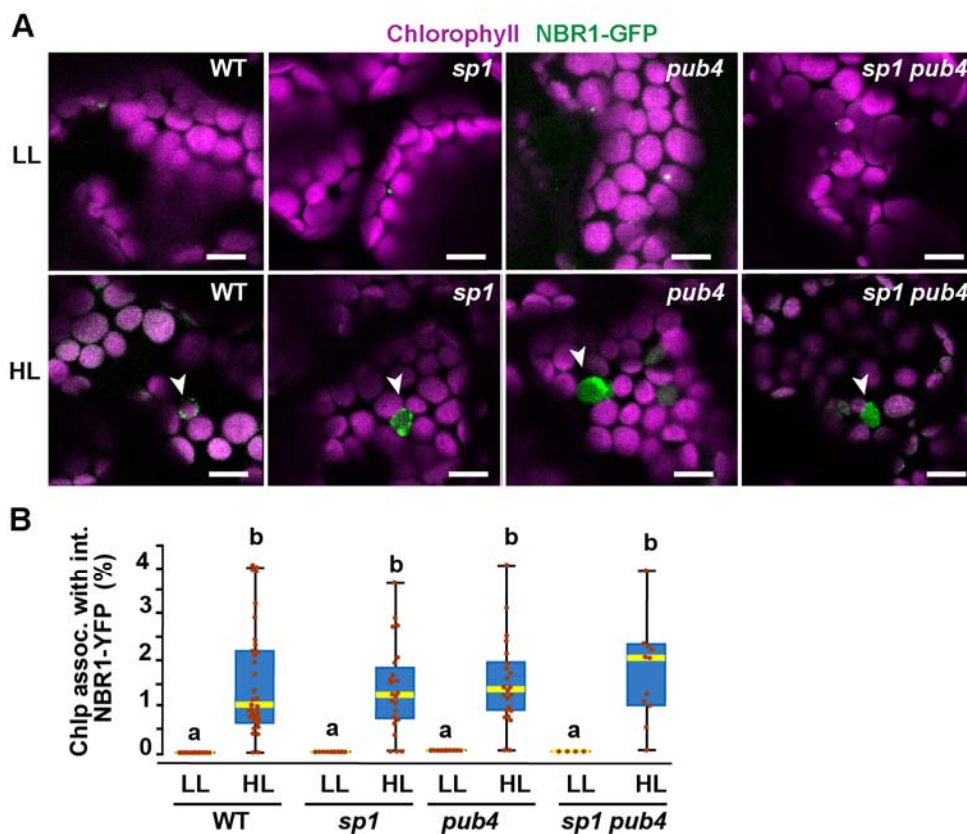
478 **(C)** Box and whisker plots show the percentages of chloroplast associated with the YFP-labeled mutated  
 479 NBR1 proteins, localized to either coats (orange) or inside chloroplasts (green). Boxes show the variation  
 480 in data through quartiles; the middle line indicates the median and whiskers show the upper and lower  
 481 fences. Different letters denote significant differences from each other based on two-way ANOVA  
 482 followed by Tukey's test ( $p < 0.05$ ).

483 Scale bars: 10  $\mu$ m in B.

484

485 **The E3 ligases PUB4 and SP1 are not required for NBR1 association with photodamaged**  
486 **chloroplasts.**

487 Since the UBA2 ubiquitin-binding domain of NBR1 is critical for chloroplast association upon HL  
488 treatment, we expressed NBR1-GFP in mutants lacking the E3 ligases PUB4 and SP1, which  
489 have been shown to ubiquitylate chloroplast envelope proteins after photoradiation damage as  
490 part of the CHLORAD pathway (Ling et al., 2012; Woodson et al., 2015). NBR1-GFP localized  
491 to photodamaged chloroplasts in *pub4-2* and *sp1-2* single and double mutants during recovery  
492 after HL (Fig. 8), suggesting that at least these two E3 ligases are not critical for NBR1  
493 association with photodamaged chloroplasts.



494

495 **Figure 8: NBR1 association with chloroplasts in mutants lacking SP1 and PUB4 E3**  
496 **ligases.**

497 **(A)** Confocal imaging of NBR1-GFP in wild type (*Col-0*), *sp1*, *pub4*, and *sp1 pub4* 8-day old  
498 seedlings under LL and 24 h after HL exposure. Arrowheads indicate chloroplasts decorated  
499 with NBR1-GFP.

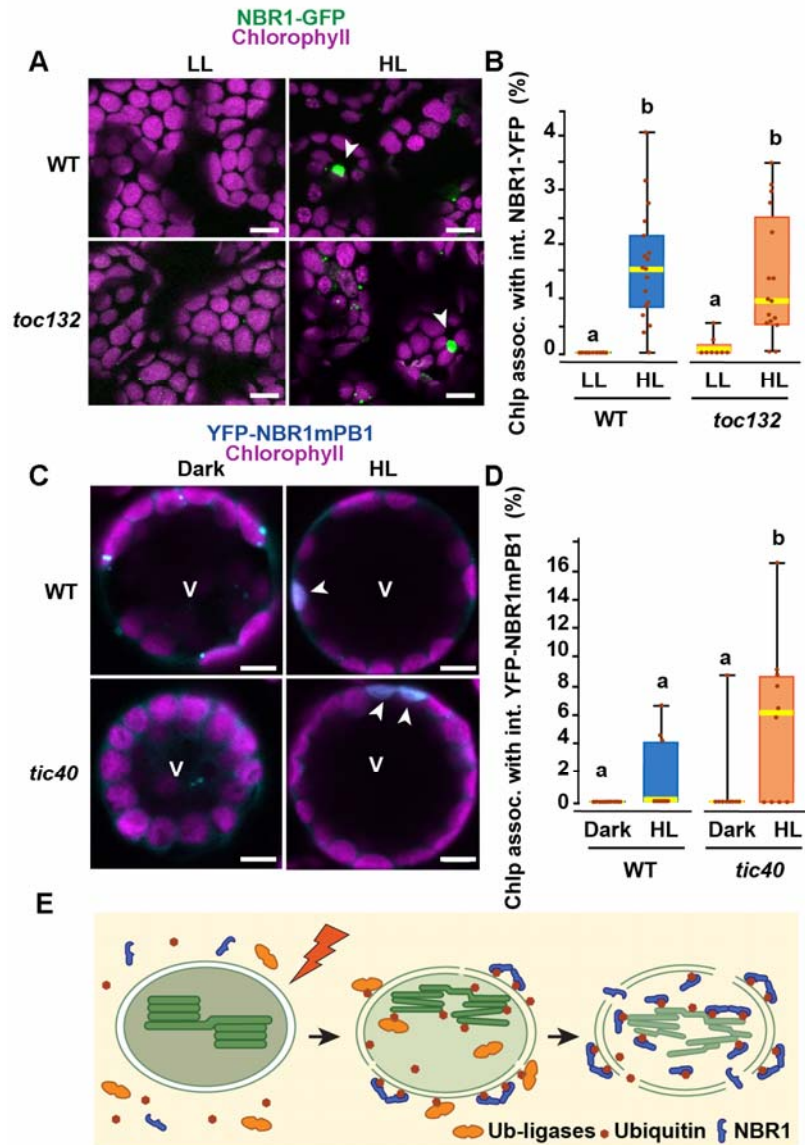
500 **(B)** Box and whisker plots show the percentage of chloroplast associated with NBR1-GFP under  
501 LL and 24 h after HL treatment. Boxes show the variation in data through quartiles; the middle  
502 line indicates the median and whiskers show the upper and lower fences. Different letters  
503 denote significant differences from each other based on two-way ANOVA followed by Tukey's  
504 test ( $p < 0.05$ ).

505 Scale bar: 10  $\mu$ m in A.

506  
507 **Fully functional TIC-TOC complexes are not required for NBR1 internalization into**  
508 **chloroplasts.**

509 To test whether NBR1 is translocated into the chloroplast stroma *via* the TIC-TOC complexes,  
510 we expressed NBR1-GFP in the transcript-null *toc132-2* mutant, which is defective in the import  
511 of a subset of chloroplast proteins (Kubis et al., 2004). The *toc132-2* mutation did not affect the  
512 association of NBR1-GFP with chloroplasts or its localization into the chloroplast lumen (Fig. 9A,  
513 B).

514 As the *toc132-2* mutation affects the translocation of only some but not all chloroplast  
515 proteins into the stroma (Kubis et al., 2004), we also tested NBR1 localization in the transcript-  
516 knockout *tic40-4* mutant, which is severely deficient in chloroplast protein import and  
517 consistently develops structurally abnormal chloroplasts (Kovacheva et al., 2005). We isolated  
518 protoplasts from 3-week old *tic40-4* and wild-type seedlings and transfected them with the  
519 *pUBN-NBR1mPB1* vector, since the NBR1mPB1 protein is internalized into photodamaged  
520 chloroplasts at a higher rate than the wild-type NBR1 protein (Fig. 7C). We exposed the  
521 transfected protoplasts to HL for 2 h and imaged them 12 h later. We found that YFP-  
522 NBR1mPB1 successfully internalized into photodamaged chloroplasts in *tic40-4* mutant  
523 protoplasts. In fact, we detected a larger proportion of chloroplasts with internal YFP-  
524 NBR1mPB1 signal in the *tic40-4* compared to wild-type protoplasts (Fig 9. C, D). Taken  
525 together, these results suggest that the TIC-TOC complex is not required for the internalization  
526 of NBR1 into chloroplasts after HL exposure.



527

528 **Figure 9. The TIC-TOC translocon is not required for the internalization of NBR1 into**  
 529 **photodamaged chloroplasts.**

530 **(A)** Confocal imaging of NBR1-GFP in wild-type Col-0 (WT) and *toc132* cotyledon mesophyll cells from 1-  
 531 week old seedlings grown under LL or at 24 h after HL exposure. Arrowheads indicate chloroplasts with  
 532 internal NBR1-GFP signal.

533 **(B)** Box and whisker plot displaying the percentages of chloroplasts associated with NBR1-GFP signal in  
 534 WT and *toc132* mutant mesophyll cells under LL or at 24h after HL exposure. Between 9 and 18 confocal  
 535 images of at least 3 cotyledons were used for quantification.

536 **(C)** Protoplasts from 3-week-old wild-type Col-0 (WT) and *tic40-4* expressing YFP-NBR1mPB1.  
537 Protoplasts were left in the dark or exposed to HL for 2 h and imaged 12 h later. Arrowheads indicate  
538 chloroplasts with internal YFP-mPB1-NBR1 signal. V, vacuole.

539 **(D)** Box and whisker plot displaying the percentages of wild type and *tic40-4* chloroplasts associated with  
540 YFP-mPB1-NBR1 signal in WT and *tic40-4* mutant protoplasts kept in dark conditions or exposed to HL  
541 and left to recover for 12 h. Between 9 and 10 protoplasts of each genotype and condition were used for  
542 quantification.

543 In B and D, boxes show the variation in data through quartiles; the middle line indicates the median and  
544 whiskers show the upper and lower fences. Different letters denote significant differences from each  
545 other based on two-way ANOVA followed by Tukey's test ( $p < 0.05$ ).

546 **(E)** Diagram summarizing a proposed mechanism for NBR1 association with photodamaged chloroplasts.  
547 HL exposure induces the breakdown of the chloroplast envelopes allowing the cytosolic ubiquitylation  
548 machinery to reach the stroma and thylakoids of photodamaged chloroplasts. As stromal and thylakoidal  
549 proteins become ubiquitylated, NBR1 diffuses into damaged chloroplasts and bind ubiquitylated proteins  
550 through its UBA2 domain. NBR1-decorated photodamaged chloroplasts are then delivered to the vacuole  
551 by microautophagy independently of ATG7.

552 Scale bars: 5  $\mu$ m in A and C.

553

## 554 **Discussion**

555 Here, we present evidence that the selective autophagy receptor NBR1 is recruited to  
556 photodamaged chloroplasts, mediating their clearance by a microautophagy-like event that is  
557 independent of the canonical ATG machinery (Figs. 1-4). Upon photoradiation damage, NBR1  
558 first becomes associated with the chloroplast surface to be later internalized into the chloroplast  
559 stroma (Fig. 1E). The association of NBR1 with chloroplasts requires its ubiquitin-binding UBA2  
560 domain whereas NBR1 internalization into the chloroplast stroma is negatively regulated by its  
561 self-polymerization PB1 domain (Fig. 7). The relocation of NBR1 into the chloroplast stroma  
562 does not rely on a functional TIC-TOC complex (Fig. 9). We hypothesize that the rupture of the  
563 outer and inner envelopes in photodamaged chloroplasts (Fig. 2C) allows for the diffusion of the  
564 ubiquitylation machinery and NBR1 from the cytosol into the chloroplast lumen, promoting  
565 ubiquitylation of both stroma and thylakoid proteins and their subsequent binding to NBR1 (Fig  
566 9E).

567

568 **NBR1 as a ubiquitin-binding chlorophagy receptor.**



569 NBR1 is a well-known aggrephagy receptor that recognizes and sorts ubiquitylated cargo for  
570 vacuolar clearance (Rasmussen et al., 2022). In plants, the formation of ubiquitylated cargo  
571 aggregates by NBR1 depends on its self-oligomerizing PB1 domain and its ubiquitin-binding  
572 capacity through the UBA2 domain (Svenning et al., 2011; Zientara-Rytter and Sirko, 2014).  
573 The AIM domain of NBR1 mediates its interaction with ATG8 and its sequestration into  
574 autophagosomes for vacuolar degradation (Svenning et al., 2011). Our studies found that, upon  
575 high photoradiation exposure, NBR1 associates with a population of photodamaged  
576 chloroplasts via a process dependent on its UBA2 domain, which then enables the association  
577 of NBR1 with both the surface of the chloroplast and its lumen (stroma and thylakoids).

578 A simple scenario based on past studies is that NBR1 binds ubiquitylated substrates of  
579 the E3 ligases PUB4 and SP1, which ubiquitylate chloroplast envelope proteins as part of the  
580 CHLORAD pathway (Ling et al., 2012; Woodson et al., 2015). However, we found that a mutant  
581 lacking both PUB4 and SP1 activity showed normal recruitment of NBR1 to photodamaged  
582 chloroplasts (Fig. 8). Recent reports have shown that most chloroplast proteins, including those  
583 localized to stroma and thylakoids are ubiquitylated for subsequent break down by the  
584 proteasomes (Li et al., 2022; Sun et al., 2022b), but how such ubiquitylation might occur inside  
585 chloroplasts was unresolved. As rupture of the chloroplast envelope membranes is a known  
586 consequence of damaging photoradiation (Nakamura et al., 2018), it is important to note our  
587 observations that NBR1 heavily decorates the surface, stroma, and thylakoids of photodamaged  
588 chloroplasts with structurally disrupted envelopes (Fig. 2E, F). Consequently, we hypothesize  
589 that the loss of envelope structural integrity allows the cytosolic ubiquitylation machinery to  
590 access the stroma and thylakoid of compromised chloroplast thus directing the massive  
591 ubiquitylation of chloroplast proteins for recognition by the NBR1 receptor. Although  
592 ubiquitylation of intra-chloroplast proteins has been connected to degradation by the 26S  
593 proteasome through CHLORAD (Li et al., 2022; Sun et al., 2022b), it is possible that remaining  
594 ubiquitylated chloroplast ghost membranes coated with NBR1 are delivered to the vacuole by  
595 microautophagy.

596 The mPB1 domain of NBR1 is necessary for aggrephagy in plants as it mediates the  
597 formation of ubiquitylated cargo accretions (Svenning et al., 2011). Here, we show that an  
598 NBR1 protein unable to oligomerize is relocated into the chloroplast lumen at a higher frequency  
599 than the wild-type NBR1 protein (Fig. 7B, C). We hypothesize that monomeric NBR1 proteins  
600 can diffuse more easily through disrupted envelope membranes and reach the chloroplast  
601 stroma where they bind ubiquitylated chloroplast proteins.

602 Surprisingly, although NBR1 targets photodamage chloroplasts for vacuolar clearance,  
603 this process requires neither its ATG8-interacting AIM domain nor ATG7, and thus independent  
604 of canonical autophagy. Although microautophagy of ATG8-decorated chloroplasts upon  
605 radiation damage requires the core ATG machinery that assembles the ATG8-PE adduct (Izumi  
606 et al., 2017), microautophagy of chloroplasts damaged by oxidative stress does not (Lemke et  
607 al., 2021). Thus, as a protein targeting chloroplasts for non-canonical microautophagy, it is  
608 possible that NBR1 also mediates the clearance of chloroplast damaged by oxidative stress.

609 Autophagy defective maize (*atg12*) and Arabidopsis (*atg2*, *atg5*, *atg7*, and *atg9*) mutant  
610 plants show reduced abundance of chloroplast proteins in different developmental and  
611 environmental conditions (McLoughlin et al., 2018; Wijerathna-Yapa et al., 2021), despite  
612 autophagy being a catabolic pathway. This could be attributed to either a lower nutrient  
613 availability in autophagy defective lines, which results in lower protein biosynthesis, or the  
614 induction of alternative proteolytic pathways to compensate for the lack of autophagy. Here, in  
615 the absence of nutritional deficiency, we also observed a lower abundance of chloroplast  
616 proteins for all autophagy defective lines (*atg7*, *nbr1*, and *nbr1 atg7*) after HL exposure (Fig 6B),  
617 consistent with either the induction of other proteolytic route(s) and/or a delay in chloroplast  
618 protein synthesis and recovery after photoradiation damage. In this context, both *nbr1* and *nbr1*  
619 *atg7* plants, showed a lessened reduction in chloroplast protein abundance relative to *atg7* (Fig  
620 6B). We speculate that all these lines display enhanced degradation of chloroplast proteins, but  
621 mutations in *NBR1* dampen this exacerbated catabolic activity that target chloroplasts when  
622 autophagy is blocked.

623 The role of NBR1 in organelle turnover and remodeling does not seem to be general for  
624 all organelles as peroxisomal protein abundance was not altered in *nbr1* backgrounds but  
625 significantly elevated in the *atg7* mutant (Fig. 6-figure supplement 2). This also confirms  
626 previous reports that, different from animals (Deosaran et al., 2013), plants do not seem to  
627 employ NBR1 for autophagic removal of peroxisomes (pexophagy) (Young et al., 2019; Jung et  
628 al., 2020).

629

### 630 **The many pathways promoting chloroplast remodeling and degradation.**

631 Chloroplast proteostasis is critical for plant survival, which is constantly challenged by  
632 daily exposure to damaging reactive oxygen species generated by the photosynthetic  
633 machinery (Foyer, 2018) and by a hypersensitivity of chloroplasts to biotic and abiotic stresses  
634 (Nishimura et al., 2017; Song et al., 2021; Wang et al., 2022). A failure to control chloroplast

635 protein turnover is often very deleterious to plants (Rowland et al., 2022). Not surprisingly  
636 considering the complexity of the organelle and its functions, chloroplast remodeling and  
637 turnover are intricate processes that integrates multiple and likely redundant or partially  
638 redundant pathways. Besides chloroplast proteases that can locally degrade proteins inside  
639 chloroplasts (Nishimura et al., 2017; Rowland et al., 2022), several autophagy and non-  
640 autophagic pathways mediate vacuolar clearance of chloroplast components (Otegui, 2018;  
641 Kikuchi et al., 2020; Rowland et al., 2022). At least three flavors of ATG8-dependent piecemeal  
642 autophagy of chloroplasts have been characterized: Rubisco-containing bodies (Chiba et al.,  
643 2003; Ishida et al., 2008; Spitzer et al., 2015), ATG8-INTERACTING PROTEIN 1 bodies  
644 (Michaeli et al., 2014), and small starch-like granule bodies (Wang et al., 2013). In addition,  
645 microautophagy of whole damaged chloroplasts occurs through at least two pathways, one  
646 dependent and the other independent of canonical autophagy (Izumi et al., 2017; Lemke et al.,  
647 2021). For the latter pathway, we provide evidence for a novel microautophagic route that  
648 requires NBR1 but not ATG8 lipidation.

649 How exactly all these pathways coordinate the remodeling and degradation of damaged  
650 chloroplasts is unclear. Upon HL exposure, we observed chloroplasts associated with either  
651 ATG8 and NBR1 as organelle cargo for canonical autophagy-dependent and independent  
652 microautophagy, respectively (Fig. 3). Only a very low proportion of chloroplasts were coated  
653 with both ATG8 and NBR1, supporting the notion that there are two separate microautophagy  
654 pathways for chloroplast clearance. However, we noticed a higher proportion of NBR1-  
655 decorated chloroplasts in HL-exposed *atg7* mutant seedlings compared to controls (Figs. 1F  
656 and 4C), consistent with the idea that photodamaged chloroplasts that are not successfully  
657 repaired or degraded by canonical autophagy, become substrates of NBR1. Interestingly, the  
658 *tic40-4* mutant that contains structurally abnormal chloroplasts (Kovacheva et al., 2005) also  
659 shows increased association of chloroplasts with NBR1 upon HL exposure (Fig. 9C), consistent  
660 with more widespread photodamage in the *tic40-4* chloroplasts, which in turn results in more  
661 chloroplasts being targeted by NBR1.

662 We had anticipated that an *nbr1 atg7* double mutant exposed to HL would show more  
663 pronounced defects in chloroplast homeostasis after HL exposure than the single mutants if the  
664 ATG8- and NBR1-mediated microautophagy pathways were both disrupted. However, the *nbr1*  
665 *atg7* double mutant did not show more drastic phenotypic alterations as compared to those  
666 seen in the single mutants in terms of both chlorophyll mean intensities and chloroplast  
667 proteome profiles, and instead, the mutant behaves either as intermediate between the two

668 single mutants or more similarly to the *atg7* single mutant. This disconnection suggests that  
669 canonical autophagy controls the main pathway for clearance of photodamaged chloroplasts,  
670 whereas NBR1 targets a relatively small population of chloroplasts and chloroplast proteins that  
671 fail to be degraded via either CHLORAD or canonical autophagy.

672

## 673 **Methods and Materials**

### 674 **Plant materials and growth conditions**

675 *Arabidopsis thaliana* seeds of *atg7-2* (GABI\_655B06) (Chung et al., 2010), *nbr1-1*  
676 (SALK\_135513) (Zhou et al., 2013), *nbr1-2* (GABI\_246H08) (Zhou et al., 2013), *atg7-2 nbr1-2*  
677 (Jung et al., 2020), *toc132-2* (SAIL\_667\_04) (Kubis et al., 2004), *tic40-4* (SAIL\_192\_C10)  
678 (Kovacheva et al., 2005), *Pro35S:mCherry-NBR1* (Svenning et al., 2011), *ProUBQ10:mCherry-*  
679 *NBR1* (Jung et al., 2020), *ProNBR1:NBR1-GFP* (Hafren et al., 2017; Thirumalaikumar et al.,  
680 2021), *Pro35S:RECA-GFP* (Kohler et al., 1997; Spitzer et al., 2015) were previously  
681 characterized. The *sp1-2* (SALK\_063571) (Ling et al., 2012) and *pub4-2* (SALK\_054373)  
682 (Woodson et al., 2015) mutant lines were acquired from Arabidopsis Biological Resource Center  
683 (<https://abrc.osu.edu/>) and *sp1-2 pub4-2 ProNBR1:NBR1-GFP* was generated by crossing.  
684 Primers used for genotyping the lines above are listed in Supplemental table 14.

685 To fuse YFP to NBR1 mutant variants, NBR1, NBR1mPB, NBR1mAIM, and  
686 NBR1 $\Delta$ UBA2 were cloned into the Gateway entry vector pDONR221 by the BP Clonase II  
687 reactions (Thermo Fisher Scientific) using Gateway expression vectors previously described  
688 (Hafren et al., 2017). The resulting entry clones were recombined with pUBN-DEST-YFP  
689 (Grefen et al., 2010) via the LR Clonase II reaction (Thermo Fisher Scientific) to generate the  
690 expression vectors with YFP. The sequences were confirmed by Sanger sequencing with YFP  
691 and NBR1 primers. The expression vectors were introduced into *Agrobacterium tumefaciens*  
692 strain GV3101. *Agrobacterium* transformants were used to transform *nbr1-2* or *atg7-2 nbr1-2*  
693 mutants by the floral dip method (Clough and Bent, 1998). T1 plants were selected on the  
694 media supplemented with 10 mg/L Basta.

695 Seeds were surface-sterilized in 10% (v/v) bleach and 1% (v/v) Triton X-100 solution for  
696 30 min and washed in distilled water at least five times. Seeds were sown on solid media  
697 containing 0.5x Murashige & Skoog salts (MS), 1% (w/v) sucrose and 0.6% Phytigel and  
698 stratified at 4°C for 2-5 days before germination. Plants were grown in growth chambers at 22°C  
699 under 16 h of light (40  $\mu\text{mol m}^{-2} \text{s}^{-1}$ ) and 8 h of dark cycle (LL). For high-light treatment (HL), 8-

700 d-old seedlings were exposed to 2000 W LED lights ( $1500 \mu\text{mol m}^{-2} \text{s}^{-1}$ ) at 12°C for 2 hours  
701 followed by recovery for the indicated time.

## 702 703 **Transient expression in Arabidopsis leaf protoplasts**

704  
705 Isolation and transformation of Arabidopsis leaf protoplasts were performed as previously  
706 described (Yoo et al., 2007) with some modifications. Briefly, rosette leaves from 3-week-old  
707 Arabidopsis wild type (Col-0) and *tic40-4* (Kovacheva et al., 2005) plants were used for  
708 protoplast isolation. Protoplasts were released in enzyme solution (20 mM MES pH 5.7, 1.5%  
709 [w/v] cellulase R10, 0.4% [w/v] macerozyme R10, 0.4 M mannitol and 20 mM KCl, 10 mM  
710  $\text{CaCl}_2$ , and 0.1% BSA) for 1 h and collected by centrifugation at 100 g for 5 min. Protoplasts  
711 were washed twice with W5 buffer (2 mM MES [pH 5.7] containing 154 mM NaCl, 125 mM  
712  $\text{CaCl}_2$  and 5 mM KCl). Then, 7  $\mu\text{g}$  of the *pUBN-YFP-NBR1mPB* vector was used for each  
713 transformation with polyethylene glycol. After transformation, the protoplasts were incubated at  
714 22 °C under dark for 2 h. For HL treatment, the transformed protoplasts were exposed to 1,500  
715  $\mu\text{mol m}^{-2} \text{s}^{-1}$  at 12°C for 2 h followed by recovery in the dark at 22°C. Control protoplasts were  
716 kept under dark conditions at 22 °C until imaging.

717 For confocal imaging, protoplasts were loaded onto an 18 Well Flat m-Slide (Ibidi).  
718 Images were captured on a Zeiss LSM 780 confocal microscope with a 63x water immersion  
719 objective. YFP was excited with a 488 nm laser and detected using a 493–527 nm band-pass  
720 filter; chlorophyll was excited with a 633 nm laser and detected using a 642–695 nm band-pass  
721 filter. Between 9 and 10 protoplasts were used for quantification of each condition and  
722 phenotype.

## 724 **Light microscopy and image analysis**

725 Confocal images were obtained in a Zeiss LSM 710 with a 40x objective (LD C-Apochromat NA  
726 = 1.2 water immersion, Carl Zeiss). GFP, YFP, and chlorophyll were excited using a 488 nm  
727 laser and emission was collected from 450 to 560 nm for GFP/YFP and from 650 to 710 nm for  
728 chlorophyll. mCherry was excited using a 561 nm laser and emission collected from 570 to 640  
729 nm. Quantification of confocal images was done with FIJI (Schindelin et al., 2012). To verify  
730 the specificity of the fluorescence signals, the emission spectra resulting from 488-nm excitation  
731 were collected between 420 and 720 nm using the lambda scan mode.

732 Multiphoton images were collected using a Nikon 40x water-immersion objective lens  
733 (1.25 NA, CFI Apochromat Lambda S 40XC WI) on an Ultima IV multiphoton microscope  
734 (Bruker FM). Chlorophyll was imaged using 890 nm multiphoton excitation from an Insight laser  
735 (Spectra Physics) and fluorescence emission was filtered using a dichroic cube filter set  
736 (720nm, 630/69 nm, Chroma Technologies). Using manual estimation of leaf size and  
737 volumetric scanning from the surface to 100 microns deep, regions of interests were chosen  
738 and imaged. A hybrid photomultiplier tube (HPM-40, Becker&Hickl GmbH) detector was  
739 deployed in photon counting mode using a fast electronic board (SPC-150, Becker&Hickl  
740 GmbH), and Prairie View (Bruker FM) software. In presence of GFP markers, a second channel  
741 was imaged using a bialkali detector with 535/50 filter (Chroma Technologies).

742 The fluorescence images were made to 2D, using a maximum intensity projection and  
743 then 2D segmentation methods were applied to identify single chloroplasts. Cellpose 2.0.5  
744 (Nucleus-model) with GPU acceleration (NVIDIA GeForce RTX 2080 Ti) generated robust  
745 chloroplast masks, which were then processed using Python (v3.9.12, Python Software  
746 Foundation) to calculate single chloroplast intensity and other morphological traits (Stringer et  
747 al., 2021)

748

#### 749 **Protein preparation for western blots**

750 Whole 8-day-old Arabidopsis seedlings were frozen with liquid nitrogen and homogenized in  
751 protein extraction buffer (150 mM Tris-HCl (pH7.5), 150 mM NaCl, 10 mM MgCl<sub>2</sub>, 10% [v/v]  
752 glycerol, 2% [w/v] polyvinylpyrrolidone, 3 mM dithiothreitol, 2 mM phenylmethylsulfonyl fluoride,  
753 0.1% [v/v] Triton X-100, 1x protease inhibitor cocktail), and centrifuged at 25,000 g for 10 min at  
754 4°C. The supernatants were mixed with 0.25 volumes of 5x SDS-PAGE sample buffer  
755 containing 10% [v/v] 2-mercaptoethanol and boiled before subjecting them to SDS-PAGE gel  
756 followed by immunoblotting with the indicated antibodies.

757

#### 758 **Protein preparation for mass spectrometry (MS) analysis.**

759 Seven-day-old wild type (Col-0), *nbr1-2*, *atg7-2*, and *nbr1-2 atg7-2* Arabidopsis seedlings were  
760 either grown under LL or left to recover for 24h after HL exposure as explained above. Whole  
761 seedlings were frozen in liquid nitrogen and grinded; protein extraction buffer (50 mM HEPES  
762 pH7.5, 5 mM Na<sub>2</sub> EDTA, 2mM DTT, 1x protease inhibitor cocktail) was added to the samples.  
763 After mixing, samples were left on ice for 15 min, and transferred to a homogenizer for gentle

764 homogenization. The homogenate was left on ice for 15 min and centrifuged at 14,000 g for 1  
765 min at 4°C; 150 µL of the supernatant was transferred to clean 1.5mL plastic tubes, mixed well  
766 by vortexing with 600 µL methanol and 150 µL chloroform. Then, 450 µL milliQ water was  
767 added to the sample and mixed by vortexing, followed by centrifugation at 14,000 g for 2 min.  
768 The top aqueous layer was removed and the proteins in the interphase collected with a pipette  
769 and transferred to a clean plastic tube followed by addition of 400 µL methanol, vortexing, and  
770 centrifugation at 14,000 g for 3 min. Methanol was removed from the tube without disturbing the  
771 pellet, which was left to dry in a vacuum concentrator.

772

### 773 **Liquid chromatography-tandem MS (LC-MS/MS).**

774 Protein pellets were resuspended in 100 µL of 8M urea. Then, 100 µg protein of each sample  
775 was reduced for 1h at room temperature with 10 mM dithiothreitol, followed by alkylation with 20  
776 mM iodoacetamide (IAA) for 1h. The reaction was quenched with 20 mM dithiothreitol (DTT)  
777 and diluted with 900 µL 25 mM ammonium bicarbonate to reduce the urea concentration below  
778 1 M, digested overnight at 37°C in the presence of 1.5 µg of sequencing grade modified trypsin  
779 (Promega). The resulting peptides were vacuum-dried in a vacuum concentrator to  
780 approximately 200 µL, acidified with 10% trifluoroacetic acid (TFA) (pH < 3), desalted and  
781 concentrated on a 100-µL Bond Elut OMIX C18 pipette tip (Agilent Technologies A57003100)  
782 according to the manufacturer's instructions. Peptides were eluted in 50 µL of 75% acetonitrile,  
783 0.1% acetic acid, vacuum-dried, and resuspended in 15 µL 5% acetonitrile, 0.1% formic acid.

784 Nanoscale liquid chromatography (LC) separation of tryptic peptides was performed on a  
785 Dionex Ultimate 3000 Rapid Separation LC system (Thermo Fisher). Peptides were loaded  
786 onto a 20 µL nanoViper sample loop (Thermo Fisher) and separated on a C18 analytical column  
787 (Acclaim PepMap RSLC C18 column, 2 µm particle size, 100 Å pore size, 75 µm × 25 cm,  
788 Thermo Fisher) by the application of a linear 2 h gradient from 4% to 45% acetonitrile in 0.1%  
789 formic acid, with a column flow rate set to 250 nL/min. Analysis of the eluted tryptic peptides  
790 was performed online using a Q Exactive Plus mass spectrometer (Thermo Scientific)  
791 possessing a Nanospray Flex Ion source (Thermo Fisher) fitted with a stainless steel nano bore  
792 emitter operated in positive electrospray ionization (ESI) mode at a capillary voltage of 1.9 kV.  
793 Data-dependent acquisition of full MS scans within a mass range of 380–1500 m/z at a  
794 resolution of 70,000 was performed, with the automatic gain control (AGC) target set to  $3.0 \times$   
795  $10^6$ , and the maximum fill time set to 200 ms. High-energy collision-induced dissociation (HCD)  
796 fragmentation of the top eight most intense peaks was performed with a normalized collision

797 energy of 28, with an intensity threshold of  $4.0 \times 10^4$  counts and an isolation window of 3.0 m/z,  
798 excluding precursors that had an unassigned, +1 or >+7, charge state. MS/MS scans were  
799 conducted at a resolution of 17,500, with an AGC target of  $2 \times 10^5$  and a maximum fill time of  
800 300 ms. The resulting MS/MS spectra were analyzed using Proteome Discoverer software  
801 (version 2.5, Thermo Fisher), which was set up to search the *A. thaliana* proteome database, as  
802 downloaded from <http://www.tair.com/> (Araport11\_pep\_20220914). Peptides were assigned  
803 using SEQUEST HT (Eng et al., 1994), with search parameters set to assume the digestion  
804 enzyme trypsin with a maximum of 1 missed cleavage, a minimum peptide length of 6,  
805 precursor mass tolerances of 10 ppm, and fragment mass tolerances of 0.02 Da.  
806 Carbamidomethylation of cysteine was specified as a static modification, while oxidation of  
807 methionine and N-terminal acetylation were specified as dynamic modifications. The target  
808 false discovery rate (FDR) of 0.01 (strict) was used as validation for peptide-spectral matches  
809 (PSMs) and peptides. Proteins that contained similar peptides and that could not be  
810 differentiated based on the MS/MS analysis alone were grouped to satisfy the principles of  
811 parsimony. Label-free quantification as previously described (Silva et al., 2006) was performed  
812 in Proteome Discoverer with a minimum Quan value threshold of 0.0001 using unique peptides,  
813 and '3 Top N' peptides used for area calculation. All samples were injected in two technical  
814 duplicates, and the protein abundances reflected the average of two technical replicates if  
815 proteins were detected in two technical replicates or used directly if the proteins were only  
816 detected in one technical replicate. Protein abundances were normalized using the median  
817 values of 150 proteins considered the least variable among each sample. The mass  
818 spectrometry proteomics data have been deposited to the ProteomeXchange Consortium *via*  
819 the PRIDE partner repository (Perez-Riverol et al., 2019) with the dataset identifier PXD039183.

820 Using the Perseus platform (Tyanova et al., 2016), intensity values from mass  
821 spectrometry were  $\log_2$  imputed and missing values were replaced with random numbers from a  
822 Gaussian distribution with a width of 0.3 and a downshift of 1.8. Statistical significance was  
823 determined using *t*-tests. Only proteins with at least 2 peptide spectral matches (one is the  
824 unique peptide) were selected for further analysis.

825

## 826 **Electron microscopy and immunogold labeling.**

827 Wild type (Col-0), *atg7-2*, and *nbr1-2* seedlings were germinated in liquid media containing 0.5x  
828 MS and 1% sucrose. Eight-day-old cotyledons either grown under LL or at 24 h after HL  
829 exposure were cut into small pieces and frozen in a high-pressure freezer (Leica EM Ice). To



830 analyze the ultrastructure of chloroplasts, the samples were freeze-substituted in 2% (w/v)  
831 osmium tetroxide in acetone on dry ice overnight; samples were adjusted to room temperature  
832 on a rocker. After several rinses with acetone, the samples were infiltrated with Epon resin  
833 (Electron Microscopy Sciences) with increasing the concentration of Epon 10% (v/v), 25%, 50%,  
834 75% in acetone, followed by three exchanges with 100% Epon. The samples were embedded  
835 and polymerized at 60°C for 24 h. For immunogold labeling, the high-pressure-frozen samples  
836 were freeze-substituted in 0.2% glutaraldehyde with 0.2% uranyl acetate in acetone at -90°C in  
837 an automated freeze-substitution device (Leica AFS). After 3 days, the temperature was raised  
838 at 5°C/h to -60°C and the samples were rinsed with precooled acetone three times and  
839 infiltrated with 30%, 60%, and 100% HM20 (Electron Microscopy Sciences) in acetone and  
840 polymerized under UV light at -50°C. Sections were blocked with 5% (w/v) solution of nonfat  
841 milk in PBS (phosphate buffered saline) containing 0.1% Tween-20 (blocking solution) for 20  
842 min, incubated with anti-NBR1 antibodies in the blocking solution (1:10) for 1 h, rinsed 3 times  
843 with PBS containing 0.5% Tween-20, and incubated with anti-rabbit secondary antibody  
844 conjugated to gold particles (Electron Microscopy Sciences) in the blocking solution for 1 h.  
845 After 3 rinses with the PBS containing 0.5% Tween-20 and another rinse with water, the  
846 samples were imaged with a transmission electron microscope (Thermo Fisher Scientific Talos).

847

#### 848 **Chloroplast isolation.**

849 Intact chloroplasts were isolated as previously described with some modifications (Kley et al.,  
850 2010; Lung et al., 2015). Four-week-old leaves were punched repeatedly with a 1 ml pipette tip  
851 in buffer (0.3 M sorbitol, 50 mM HEPES/KOH [pH 7.5], 5 mM ethylenediaminetetraacetic acid  
852 [EDTA], 5 mM ethyleneglycoltetraacetic acid [EGTA], 1 mM MgCl<sub>2</sub>, 10 mM NaHCO<sub>3</sub>, and 0.5  
853 mM dithiothreitol) and filtered through cheesecloth. The filtrate was carefully loaded onto a two-  
854 step Percoll gradient that was prepared by overlaying 40% Percoll buffer on top of 85% Percoll  
855 and centrifuged for 20 min at 2,000 g in a swing out rotor, brakes set off. The upper layer of the  
856 40% Percoll containing broken chloroplasts was discarded, and the intact chloroplasts at the  
857 interface of the Percoll layers was collected and washed 5 times by adding buffer and  
858 centrifuged for 5 min at 1,000 g. Isolated chloroplasts were resuspended in buffer. We then  
859 added 0.25 volumes of 5x SDS-PAGE sample buffer containing 10% (v/v) 2-mercaptoethanol to  
860 the samples. Protein extracts were subjected to SDS-PAGE followed by immunoblotting with  
861 the indicated antibodies.

862

863 **Antibodies**

864 Antibodies against GFP (Chromotek), anti-PsbA/D1 (Agrisera), anti-cFBPase (Agrisera  
865 AS04043), anti-TIC40 (Agrisera), anti-Toc75 (Agrisera), anti-NBR1 (Jung et al., 2020), and  
866 histone H3 (Abcam AB1791) were obtained from the indicated sources.

867

868 **Statistical analyses**

869 T-tests were performed in Microsoft Excel. ANOVA tests followed by post-hoc Tukey were  
870 performed using the calculator at [https://astatsa.com/OneWay\\_Anova\\_with\\_TukeyHSD/](https://astatsa.com/OneWay_Anova_with_TukeyHSD/). Data  
871 was visualized using GraphPad Prism 9 and Excel. The Venn diagram shown in Fig 6 were  
872 created using <http://bioinformatics.psb.ugent.be/webtools/Venn/>.

873

874 **Accession numbers:** NBR1 (At4g24690), ATG7 (At5g45900), SP1 (At1g63900), PUB4  
875 (At2g23140), TOC132 (At2g16640), TIC40 (AT5G16620).

876

877 **Materials availability:** newly generated transgenic lines are available upon request.

878

879 **Funding:** This work was supported by grants U.S. National Science Foundation IOS-1840687  
880 to M.S.O. and R.D.V., U.S. Department of Energy grant DE-SC0019013 to MSO and KWE,  
881 National Institute of Health 1S10 OD026769-01 to MSO, and Australian Research Council  
882 (FL200100057) to AHM.

883

884 **Acknowledgements:** We would like to thank Daniel Hofius for sharing NBR1 constructs with  
885 us, Taijoon Chung for providing mutant and transgenic lines, Janice Pennington for her  
886 assistance with the electron microscopy analysis, and Dr Sarah Swanson for her support with  
887 confocal imaging.

888

889 **Competing interests:** the authors declare no competing interests.

890

891 **References**

892 **Bjørkøy, G., Lamark, T., Brech, A., Outzen, H., Perander, M., Overvatn, A., Stenmark, H.,**  
893 **and Johansen, T. (2005). p62/SQSTM1 forms protein aggregates degraded by**

- 894 autophagy and has a protective effect on huntingtin-induced cell death. *J Cell Biol* **171**,  
895 603-614.
- 896 **Cha-Molstad, H., Sung, K.S., Hwang, J., Kim, K.A., Yu, J.E., Yoo, Y.D., Jang, J.M., Han,**  
897 **D.H., Molstad, M., Kim, J.G., Lee, Y.J., Zakrzewska, A., Kim, S.H., Kim, S.T., Kim,**  
898 **S.Y., Lee, H.G., Soung, N.K., Ahn, J.S., Ciechanover, A., Kim, B.Y., and Kwon, Y.T.**  
899 (2015). Amino-terminal arginylation targets endoplasmic reticulum chaperone BiP for  
900 autophagy through p62 binding. *Nat Cell Biol* **17**, 917-929.
- 901 **Chiba, A., Ishida, H., Nishizawa, N.K., Makino, A., and Mae, T.** (2003). Exclusion of ribulose-  
902 1,5-biphosphate carboxylase/oxygenase from chloroplasts by specific bodies in naturally  
903 senescing leaves of wheat. *Plant Cell Physiol.* **44**, 914-921.
- 904 **Chung, T., Phillips, A.R., and Vierstra, R.D.** (2010). ATG8 lipidation and ATG8-mediated  
905 autophagy in *Arabidopsis* require ATG12 expressed from the differentially controlled  
906 *ATG12A* and *ATG12B* loci. *Plant J* **62**, 483-493.
- 907 **Ciuffa, R., Lamark, T., Tarafder, A.K., Guesdon, A., Rybina, S., Hagen, W.J., Johansen, T.,**  
908 **and Sachse, C.** (2015). The selective autophagy receptor p62 forms a flexible  
909 filamentous helical scaffold. *Cell Rep* **11**, 748-758.
- 910 **Clough, S.J., and Bent, A.F.** (1998). Floral dip: a simplified method for *Agrobacterium*-  
911 mediated transformation of *Arabidopsis thaliana*. *Plant J* **16**, 735-743.
- 912 **Dagdas, Y.F., Pandey, P., Tumbas, Y., Sanguankiatichai, N., Belhaj, K., Duggan, C., Leary,**  
913 **A.Y., Segretin, M.E., Contreras, M.P., Savage, Z., Khandare, V.S., Kamoun, S., and**  
914 **Bozkurt, T.O.** (2018). Host autophagy machinery is diverted to the pathogen interface to  
915 mediate focal defense responses against the Irish potato famine pathogen. *Elife* **7**,  
916 37476.
- 917 **Dagdas, Y.F., Belhaj, K., Maqbool, A., Chaparro-Garcia, A., Pandey, P., Petre, B.,**  
918 **Tabassum, N., Cruz-Mireles, N., Hughes, R.K., Sklenar, J., Win, J., Menke, F.,**  
919 **Findlay, K., Banfield, M.J., Kamoun, S., and Bozkurt, T.O.** (2016). An effector of the  
920 Irish potato famine pathogen antagonizes a host autophagy cargo receptor. *Elife* **5**,  
921 e10856.
- 922 **Deosaran, E., Larsen, K.B., Hua, R., Sargent, G., Wang, Y., Kim, S., Lamark, T., Jauregui,**  
923 **M., Law, K., Lippincott-Schwartz, J., Brech, A., Johansen, T., and Kim, P.K.** (2013).  
924 NBR1 acts as an autophagy receptor for peroxisomes. *J Cell Sci* **126**, 939-952.
- 925 **Eng, J.K., McCormack, A.L., and Yates, J.R.** (1994). An approach to correlate tandem mass  
926 spectral data of peptides with amino acid sequences in a protein database. *J Am Soc*  
927 *Mass Spectrom* **5**, 976-989.

- 928 **Foyer, C.H.** (2018). Reactive oxygen species, oxidative signaling and the regulation of  
929 photosynthesis. *Environ Exp Bot* **154**, 134-142.
- 930 **Geldner, N., Denervaud-Tendon, V., Hyman, D.L., Mayer, U., Stierhof, Y.D., and Chory, J.**  
931 (2009). Rapid, combinatorial analysis of membrane compartments in intact plants with a  
932 multicolor marker set. *Plant J* **59**, 169-178.
- 933 **Grefen, C., Donald, N., Hashimoto, K., Kudla, J., Schumacher, K., and Blatt, M.R.** (2010). A  
934 ubiquitin-10 promoter-based vector set for fluorescent protein tagging facilitates temporal  
935 stability and native protein distribution in transient and stable expression studies. *Plant J*  
936 **64**, 355-365.
- 937 **Hafren, A., Macia, J.L., Love, A.J., Milner, J.J., Drucker, M., and Hofius, D.** (2017). Selective  
938 autophagy limits cauliflower mosaic virus infection by NBR1-mediated targeting of viral  
939 capsid protein and particles. *Proc Natl Acad Sci U S A* **114**, E2026-E2035.
- 940 **Hafren, A., Ustun, S., Hochmuth, A., Svenning, S., Johansen, T., and Hofius, D.** (2018).  
941 Turnip mosaic virus counteracts selective autophagy of the viral silencing suppressor  
942 HCpro. *Plant Physiol* **176**, 649-662.
- 943 **Ichimura, Y., Kumanomidou, T., Sou, Y.S., Mizushima, T., Ezaki, J., Ueno, T., Kominami,**  
944 **E., Yamane, T., Tanaka, K., and Komatsu, M.** (2008). Structural basis for sorting  
945 mechanism of p62 in selective autophagy. *J Biol Chem* **283**, 22847-22857.
- 946 **Ishida, H., Yoshimoto, K., Izumi, M., Reisen, D., Yano, Y., Makino, A., Ohsumi, Y., Hanson,**  
947 **M.R., and Mae, T.** (2008). Mobilization of Rubisco and stroma-localized fluorescent  
948 proteins of chloroplasts to the vacuole by an ATG gene-dependent autophagic process.  
949 *Plant Physiol* **148**, 142-155.
- 950 **Izumi, M., Ishida, H., Nakamura, S., and Hidema, J.** (2017). Entire photodamaged  
951 chloroplasts are transported to the central vacuole by autophagy. *Plant Cell* **29**, 377-394.
- 952 **Jakobi, A.J., Huber, S.T., Mortensen, S.A., Schultz, S.W., Palara, A., Kuhm, T., Shrestha,**  
953 **B.K., Lamark, T., Hagen, W.J.H., Wilmanns, M., Johansen, T., Brech, A., and**  
954 **Sachse, C.** (2020). Structural basis of p62/SQSTM1 helical filaments and their role in  
955 cellular cargo uptake. *Nat Commun* **11**, 440.
- 956 **Ji, C., Zhou, J., Guo, R., Lin, Y., Kung, C.H., Hu, S., Ng, W.Y., Zhuang, X., and Jiang, L.**  
957 (2020). AtNBR1 Is a Selective Autophagic Receptor for AtExo70E2 in Arabidopsis. *Plant*  
958 *Physiol* **184**, 777-791.
- 959 **Jung, H., Lee, H.N., Marshall, R.S., Lomax, A.W., Yoon, M.J., Kim, J., Kim, J.H., Vierstra,**  
960 **R.D., and Chung, T.** (2020). Arabidopsis cargo receptor NBR1 mediates selective  
961 autophagy of defective proteins. *J Exp Bot* **71**, 73-89.

- 962 **Kikuchi, Y., Nakamura, S., Woodson, J.D., Ishida, H., Ling, Q., Hidema, J., Jarvis, R.P.,**  
963 **Hagihara, S., and Izumi, M.** (2020). Chloroplast autophagy and ubiquitination combine  
964 to manage oxidative damage and starvation responses. *Plant Physiol* **183**, 1531-1544.
- 965 **Kley, J., Heil, M., Muck, A., Svatos, A., and Boland, W.** (2010). Isolating intact chloroplasts  
966 from small *Arabidopsis* samples for proteomic studies. *Anal Biochem* **398**, 198-202.
- 967 **Kohler, R.H., Cao, J., Zipfel, W.R., Webb, W.W., and Hanson, M.R.** (1997). Exchange of  
968 protein molecules through connections between higher plant plastids. *Science* **276**,  
969 2039-2042.
- 970 **Komatsu, M., Waguri, S., Koike, M., Sou, Y.S., Ueno, T., Hara, T., Mizushima, N., Iwata, J.,**  
971 **Ezaki, J., Murata, S., Hamazaki, J., Nishito, Y., Iemura, S., Natsume, T., Yanagawa,**  
972 **T., Uwayama, J., Warabi, E., Yoshida, H., Ishii, T., Kobayashi, A., Yamamoto, M.,**  
973 **Yue, Z., Uchiyama, Y., Kominami, E., and Tanaka, K.** (2007). Homeostatic levels of  
974 p62 control cytoplasmic inclusion body formation in autophagy-deficient mice. *Cell* **131**,  
975 1149-1163.
- 976 **Kovacheva, S., Bédard, J., Patel, R., Dudley, P., Twell, D., Ríos, G., Koncz, C., and Jarvis,**  
977 **P.** (2005). In vivo studies on the roles of Tic110, Tic40 and Hsp93 during chloroplast  
978 protein import. *Plant J* **41**, 412-428.
- 979 **Kubis, S., Patel, R., Combe, J., Bédard, J., Kovacheva, S., Lilley, K., Biehl, A., Leister, D.,**  
980 **Ríos, G., Koncz, C., and Jarvis, P.** (2004). Functional specialization amongst the  
981 *Arabidopsis* Toc159 family of chloroplast protein import receptors. *Plant Cell* **16**, 2059-  
982 2077.
- 983 **Kwon, D.H., Park, O.H., Kim, L., Jung, Y.O., Park, Y., Jeong, H., Hyun, J., Kim, Y.K., and**  
984 **Song, H.K.** (2018). Insights into degradation mechanism of N-end rule substrates by  
985 p62/SQSTM1 autophagy adapter. *Nat Commun* **9**, 3291.
- 986 **Lemke, M.D., Fisher, K.E., Kozłowska, M.A., Tano, D.W., and Woodson, J.D.** (2021). The  
987 core autophagy machinery is not required for chloroplast singlet oxygen-mediated cell  
988 death in the *Arabidopsis thaliana* plastid ferrochelatase two mutant. *BMC Plant Biol* **21**,  
989 342.
- 990 **Leong, J.X., Raffener, M., Spinti, D., Langin, G., Franz-Wachtel, M., Guzman, A.R., Kim,**  
991 **J.G., Pandey, P., Minina, A.E., Macek, B., Hafrén, A., Bozkurt, T.O., Mudgett, M.B.,**  
992 **Börnke, F., Hofius, D., and Üstün, S.** (2022). A bacterial effector counteracts host  
993 autophagy by promoting degradation of an autophagy component. *EMBO J* **41**,  
994 e110352.

- 995 **Li, J., Yuan, J., Li, Y., Sun, H., Ma, T., Huai, J., Yang, W., Zhang, W., and Lin, R.** (2022). The  
996 CDC48 complex mediates ubiquitin-dependent degradation of intra-chloroplast proteins  
997 in plants. *Cell Rep* **39**, 110664.
- 998 **Ling, Q., Huang, W., Baldwin, A., and Jarvis, P.** (2012). Chloroplast biogenesis is regulated  
999 by direct action of the ubiquitin-proteasome system. *Science* **338**, 655-659.
- 1000 **Ling, Q., Broad, W., Trösch, R., Töpel, M., Demiral Sert, T., Lymperopoulos, P., Baldwin,**  
1001 **A., and Jarvis, R.P.** (2019). Ubiquitin-dependent chloroplast-associated protein  
1002 degradation in plants. *Science* **363**, eaav4467.
- 1003 **Lung, S.C., Smith, M.D., and Chuong, S.D.** (2015). Isolation of Chloroplasts from Plant  
1004 Protoplasts. *Cold Spring Harb Protoc* **2015**, 895-899.
- 1005 **McLoughlin, F., Augustine, R.C., Marshall, R.S., Li, F., Kirkpatrick, L.D., Otegui, M.S., and**  
1006 **Vierstra, R.D.** (2018). Maize multi-omics reveal roles for autophagic recycling in  
1007 proteome remodelling and lipid turnover. *Nat Plants* **4**, 1056-1070.
- 1008 **Michaeli, S., Honig, A., Levanony, H., Peled-Zehavi, H., and Galili, G.** (2014). Arabidopsis  
1009 ATG8-INTERACTING PROTEIN1 is involved in autophagy-dependent vesicular  
1010 trafficking of plastid proteins to the vacuole. *Plant Cell* **26**, 4084-4101.
- 1011 **Mizushima, N., Noda, T., Yoshimori, T., Tanaka, Y., Ishii, T., George, M.D., Klionsky, D.J.,**  
1012 **Ohsumi, M., and Ohsumi, Y.** (1998). A protein conjugation system essential for  
1013 autophagy. *Nature* **395**, 395-398.
- 1014 **Nakamura, S., Hidema, J., Sakamoto, W., Ishida, H., and Izumi, M.** (2018). Selective  
1015 elimination of membrane-damaged chloroplasts via microautophagy. *Plant Physiol* **177**,  
1016 1007-1026.
- 1017 **Nezis, I.P., Simonsen, A., Sagona, A.P., Finley, K., Gaumer, S., Contamine, D., Rusten,**  
1018 **T.E., Stenmark, H., and Brech, A.** (2008). Ref(2)P, the *Drosophila melanogaster*  
1019 homologue of mammalian p62, is required for the formation of protein aggregates in  
1020 adult brain. *J Cell Biol* **180**, 1065-1071.
- 1021 **Nishimura, K., Kato, Y., and Sakamoto, W.** (2017). Essentials of proteolytic machineries in  
1022 chloroplasts. *Mol Plant* **10**, 4-19.
- 1023 **Noda, N.N., Kumeta, H., Nakatogawa, H., Satoo, K., Adachi, W., Ishii, J., Fujioka, Y.,**  
1024 **Ohsumi, Y., and Inagaki, F.** (2008). Structural basis of target recognition by Atg8/LC3  
1025 during selective autophagy. *Genes Cells* **13**, 1211-1218.
- 1026 **Ohsumi, Y.** (2001). Molecular dissection of autophagy: two ubiquitin-like systems. *Nat Rev Mol*  
1027 *Cell Biol.* **2**, 211-216.

- 1028 **Oikawa, K., Goto-Yamada, S., Hayashi, Y., Takahashi, D., Kimori, Y., Shibata, M.,**  
1029 **Yoshimoto, K., Takemiya, A., Kondo, M., Hikino, K., Kato, A., Shimoda, K., Ueda,**  
1030 **H., Uemura, M., Numata, K., Ohsumi, Y., Hara-Nishimura, I., Mano, S., Yamada, K.,**  
1031 **and Nishimura, M.** (2022). Pexophagy suppresses ROS-induced damage in leaf cells  
1032 under high-intensity light. *Nat Commun* **13**, 7493.
- 1033 **Otegui, M.S.** (2018). Vacuolar degradation of chloroplast components: autophagy and beyond.  
1034 *J Exp Bot* **69**, 741-750.
- 1035 **Perez-Riverol, Y., Zorin, A., Dass, G., Vu, M.T., Xu, P., Glont, M., Vizcaíno, J.A., Jarnuczak,**  
1036 **A.F., Petryszak, R., Ping, P., and Hermjakob, H.** (2019). Quantifying the impact of  
1037 public omics data. *Nat Commun* **10**, 3512.
- 1038 **Rasmussen, N.L., Kournoutis, A., Lamark, T., and Johansen, T.** (2022). NBR1: The  
1039 archetypal selective autophagy receptor. *J Cell Biol* **221**, e202208092.
- 1040 **Rowland, E., Kim, J., Friso, G., Poliakov, A., Ponnala, L., Sun, Q., and van Wijk, K.J.**  
1041 (2022). The CLP and PREP protease systems coordinate maturation and degradation of  
1042 the chloroplast proteome in *Arabidopsis thaliana*. *New Phytol* **236**, 1339-1357.
- 1043 **Scheuring, D., Schöller, M., Kleine-Vehn, J., and Löffke, C.** (2015). Vacuolar staining  
1044 methods in plant cells. *Methods Mol Biol* **1242**, 83-92.
- 1045 **Schindelin, J., Arganda-Carreras, I., Frise, E., Kaynig, V., Longair, M., Pietzsch, T.,**  
1046 **Preibisch, S., Rueden, C., Saalfeld, S., Schmid, B., Tinevez, J.Y., White, D.J.,**  
1047 **Hartenstein, V., Eliceiri, K., Tomancak, P., and Cardona, A.** (2012). Fiji: an open-  
1048 source platform for biological-image analysis. *Nat Methods* **9**, 676-682.
- 1049 **Seibenhener, M.L., Babu, J.R., Geetha, T., Wong, H.C., Krishna, N.R., and Wooten, M.W.**  
1050 (2004). Sequestosome 1/p62 is a polyubiquitin chain binding protein involved in ubiquitin  
1051 proteasome degradation. *Mol Cell Biol* **24**, 8055-8068.
- 1052 **Silva, J.C., Gorenstein, M.V., Li, G.Z., Vissers, J.P., and Geromanos, S.J.** (2006). Absolute  
1053 quantification of proteins by LCMSE: a virtue of parallel MS acquisition. *Mol Cell*  
1054 *Proteomics* **5**, 144-156.
- 1055 **Song, Y., Feng, L., Alyafei, M.A.M., Jaleel, A., and Ren, M.** (2021). Function of chloroplasts in  
1056 plant stress responses. *Int J Mol Sci* **22**, 13464.
- 1057 **Spitzer, C., Li, F., Buono, R., Roschztardt, H., Chung, T., Zhang, M., Osteryoung, K.W.,**  
1058 **Vierstra, R.D., and Otegui, M.S.** (2015). The endosomal protein CHARGED  
1059 MULTIVESICULAR BODY PROTEIN1 regulates the autophagic turnover of plastids in  
1060 *Arabidopsis*. *Plant Cell* **27**, 391-402.

- 1061 **Stringer, C., Wang, T., Michaelos, M., and Pachitariu, M.** (2021). Cellpose: a generalist  
1062 algorithm for cellular segmentation. *Nat Methods* **18**, 100-106.
- 1063 **Sun, S., Feng, L., Chung, K.P., Lee, K.M., Cheung, H.H., Luo, M., Ren, K., Law, K.C., Jiang,**  
1064 **L., Wong, K.B., and Zhuang, X.** (2022a). Mechanistic insights into an atypical  
1065 interaction between ATG8 and SH3P2 in *Arabidopsis thaliana*. *Autophagy* **18**, 1350-  
1066 1366.
- 1067 **Sun, Y., Yao, Z., Ye, Y., Fang, J., Chen, H., Lyu, Y., Broad, W., Fournier, M., Chen, G., Hu,**  
1068 **Y., Mohammed, S., Ling, Q., and Jarvis, R.P.** (2022b). Ubiquitin-based pathway acts  
1069 inside chloroplasts to regulate photosynthesis. *Sci Adv* **8**, eabq7352.
- 1070 **Svenning, S., Lamark, T., Krause, K., and Johansen, T.** (2011). Plant NBR1 is a selective  
1071 autophagy substrate and a functional hybrid of the mammalian autophagic adapters  
1072 NBR1 and p62/SQSTM1. *Autophagy* **7**, 993-1010.
- 1073 **Thirumalaikumar, V.P., Gorka, M., Schulz, K., Masclaux-Daubresse, C., Sampathkumar,**  
1074 **A., Skirycz, A., Vierstra, R.D., and Balazadeh, S.** (2021). Selective autophagy  
1075 regulates heat stress memory in *Arabidopsis* by NBR1-mediated targeting of HSP90.1  
1076 and ROF1. *Autophagy* **17**, 2184-2199.
- 1077 **Turco, E., Savova, A., Gere, F., Ferrari, L., Romanov, J., Schuschnig, M., and Martens, S.**  
1078 (2021). Reconstitution defines the roles of p62, NBR1 and TAX1BP1 in ubiquitin  
1079 condensate formation and autophagy initiation. *Nat Commun* **12**, 5212.
- 1080 **Tyanova, S., Temu, T., Sinitcyn, P., Carlson, A., Hein, M.Y., Geiger, T., Mann, M., and Cox,**  
1081 **J.** (2016). The Perseus computational platform for comprehensive analysis of  
1082 (prote)omics data. *Nat Methods* **13**, 731-740.
- 1083 **Üstün, S., Hafrén, A., Liu, Q., Marshall, R.S., Minina, E.A., Bozhkov, P.V., Vierstra, R.D.,**  
1084 **and Hofius, D.** (2018). Bacteria exploit autophagy for proteasome degradation and  
1085 enhanced virulence in plants. *Plant Cell* **30**, 668-685.
- 1086 **Wang, J., Zhang, Q., Bao, Y., and Bassham, D.** (2022). Autophagic degradation of  
1087 membrane-bound organelles in plants. *Biosci Rep* **in press**.
- 1088 **Wang, Y., Yu, B., Zhao, J., Guo, J., Li, Y., Han, S., Huang, L., Du, Y., Hong, Y., Tang, D.,**  
1089 **and Liu, Y.** (2013). Autophagy contributes to leaf starch degradation. *Plant Cell* **25**,  
1090 1383-1399.
- 1091 **Wang, Y.Y., Zhang, J., Liu, X.M., Li, Y., Sui, J., Dong, M.Q., Ye, K., and Du, L.L.** (2021).  
1092 Molecular and structural mechanisms of ZZ domain-mediated cargo selection by Nbr1.  
1093 *EMBO J* **40**, e107497.



- 1094 **Wijerathna-Yapa, A., Signorelli, S., Fenske, R., Ganguly, D.R., Stroeher, E., Li, L., Pogson,**  
1095 **B.J., Duncan, O., and Millar, A.H.** (2021). Autophagy mutants show delayed  
1096 chloroplast development during de-etiolation in carbon limiting conditions. *Plant J* **108**,  
1097 459-477.
- 1098 **Woodson, J.D., Joens, M.S., Sinson, A.B., Gilkerson, J., Salome, P.A., Weigel, D.,**  
1099 **Fitzpatrick, J.A., and Chory, J.** (2015). Ubiquitin facilitates a quality-control pathway  
1100 that removes damaged chloroplasts. *Science* **350**, 450-454.
- 1101 **Xie, Z., Nair, U., and Klionsky, D.J.** (2008). Atg8 controls phagophore expansion during  
1102 autophagosome formation. *Mol Biol Cell* **19**, 3290-3298.
- 1103 **Yoo, S.D., Cho, Y.H., and Sheen, J.** (2007). Arabidopsis mesophyll protoplasts: a versatile cell  
1104 system for transient gene expression analysis. *Nat Protoc* **2**, 1565-1572.
- 1105 **Young, P.G., Passalacqua, M.J., Chappell, K., Llinas, R.J., and Bartel, B.** (2019). A facile  
1106 forward-genetic screen for Arabidopsis autophagy mutants reveals twenty-one loss-of-  
1107 function mutations disrupting six ATG genes. *Autophagy* **15**, 941-959.
- 1108 **Zhang, Y., and Chen, Z.** (2020). Broad and complex roles of NBR1-mediated selective  
1109 autophagy in plant stress responses. *Cells* **9**, 2562.
- 1110 **Zhou, J., Wang, J., Cheng, Y., Chi, Y.J., Fan, B., Yu, J.Q., and Chen, Z.** (2013). NBR1-  
1111 mediated selective autophagy targets insoluble ubiquitinated protein aggregates in plant  
1112 stress responses. *PLoS Genet* **9**, e1003196.
- 1113 **Zhou, J., Zhang, Y., Qi, J., Chi, Y., Fan, B., Yu, J.Q., and Chen, Z.** (2014). E3 ubiquitin ligase  
1114 CHIP and NBR1-mediated selective autophagy protect additively against proteotoxicity  
1115 in plant stress responses. *PLoS Genet* **10**, e1004116.
- 1116 **Zientara-Rytter, K., and Sirko, A.** (2014). Significant role of PB1 and UBA domains in  
1117 multimerization of Joka2, a selective autophagy cargo receptor from tobacco. *Front Plant*  
1118 *Sci* **5**, 13.
- 1119 **Zientara-Rytter, K., Lukomska, J., Moniuszko, G., Gwozdecki, R., Surowiecki, P.,**  
1120 **Lewandowska, M., Liszewska, F., Wawrzyńska, A., and Sirko, A.** (2011).  
1121 Identification and functional analysis of Joka2, a tobacco member of the family of  
1122 selective autophagy cargo receptors. *Autophagy* **7**, 1145-1158.

1123

1124 **Supplemental Tables**

1125 **Supplemental Table 1:** Proteins identified by at least 2 peptide spectral matches.

1126 **Supplemental Table 2:** Normalized protein abundances based on the average of two technical  
1127 replicates or used directly if the proteins were only detected in one technical replicate.

1128 **Supplemental Table 3:** Protein abundances expressed as Log2 values.

1129 **Supplemental Table 4:** Relative changes of protein abundance between LL and HL conditions  
1130 in WT plants. Analysis was performed using the Perseus platform 2.0.6.0 (Tyanova et al., 2016),  
1131 intensity values from mass spectrometry were log2 imputed and missing values were replaced  
1132 with random numbers from a Gaussian distribution with a width of 0.3 and a downshift of 1.8.  
1133 Statistical significance was determined using t-tests. The protein localizations and functions  
1134 were categorized based on the GO term listed below. GO:0006914 (Autophagy), GO:0000502  
1135 (Proteasome), GO:0009507 (Chloroplast), GO:0005739 (Mitochondria), GO:0005777  
1136 (Peroxisome), GO:0005840 (Ribosome), GO:0009941 (Chloroplast envelope), GO:0009570  
1137 (Chloroplast stroma) and GO:0009534 (Chloroplast thylakoid).

1138 **Supplemental Table 5:** Relative changes of protein abundance between LL and HL conditions  
1139 in the *atg7* mutant. Analysis was performed using the Perseus platform 2.0.6.0 (Tyanova et al.,  
1140 2016), intensity values from mass spectrometry were log2 imputed and missing values were  
1141 replaced with random numbers from a Gaussian distribution with a width of 0.3 and a downshift  
1142 of 1.8. Statistical significance was determined using t-tests. The protein localizations and  
1143 functions were categorized based on the GO term listed below. GO:0006914 (Autophagy),  
1144 GO:0000502 (Proteasome), GO:0009507 (Chloroplast), GO:0005739 (Mitochondria),  
1145 GO:0005777 (Peroxisome), GO:0005840 (Ribosome), GO:0009941 (Chloroplast envelope),  
1146 GO:0009570 (Chloroplast stroma) and GO:0009534 (Chloroplast thylakoid).

1147 **Supplemental Table 6:** Relative changes of protein abundance between LL and HL conditions  
1148 in the *nbr1* mutant. Analysis was performed using the Perseus platform 2.0.6.0 (Tyanova et al.,  
1149 2016), intensity values from mass spectrometry were log2 imputed and missing values were  
1150 replaced with random numbers from a Gaussian distribution with a width of 0.3 and a downshift  
1151 of 1.8. Statistical significance was determined using t-tests. The protein localizations and  
1152 functions were categorized based on the GO term listed below. GO:0006914 (Autophagy),  
1153 GO:0000502 (Proteasome), GO:0009507 (Chloroplast), GO:0005739 (Mitochondria),  
1154 GO:0005777 (Peroxisome), GO:0005840 (Ribosome), GO:0009941 (Chloroplast envelope),  
1155 GO:0009570 (Chloroplast stroma) and GO:0009534 (Chloroplast thylakoid).

1156 **Supplemental Table 7:** Relative changes of protein abundance between LL and HL conditions  
1157 in the *nbr1 atg7* double mutant. Analysis was performed using the Perseus platform 2.0.6.0  
1158 (Tyanova et al., 2016), intensity values from mass spectrometry were log<sub>2</sub> imputed and missing  
1159 values were replaced with random numbers from a Gaussian distribution with a width of 0.3 and  
1160 a downshift of 1.8. Statistical significance was determined using t-tests. The protein localizations  
1161 and functions were categorized based on the GO term listed below. GO:0006914 (Autophagy),  
1162 GO:0000502 (Proteasome), GO:0009507 (Chloroplast), GO:0005739 (Mitochondria),  
1163 GO:0005777 (Peroxisome), GO:0005840 (Ribosome), GO:0009941 (Chloroplast envelope),  
1164 GO:0009570 (Chloroplast stroma) and GO:0009534 (Chloroplast thylakoid).

1165 **Supplemental Table 8:** Comparison of protein abundances between WT and the *atg7* mutant  
1166 under HL conditions. Analysis was performed using the Perseus platform 2.0.6.0 (Tyanova et  
1167 al., 2016), intensity values from mass spectrometry were log<sub>2</sub> imputed and missing values were  
1168 replaced with random numbers from a Gaussian distribution with a width of 0.3 and a downshift  
1169 of 1.8. Statistical significance was determined using t-tests. The protein localizations and  
1170 functions were categorized based on the GO term listed below. GO:0006914 (Autophagy),  
1171 GO:0000502 (Proteasome), GO:0009507 (Chloroplast), GO:0005739 (Mitochondria),  
1172 GO:0005777 (Peroxisome), GO:0005840 (Ribosome), GO:0009941 (Chloroplast envelope),  
1173 GO:0009570 (Chloroplast stroma) and GO:0009534 (Chloroplast thylakoid).

1174 **Supplemental Table 9:** Comparison of protein abundances between WT and the *nbr1* mutant  
1175 under HL conditions. Analysis was performed using the Perseus platform 2.0.6.0 (Tyanova et  
1176 al., 2016), intensity values from mass spectrometry were log<sub>2</sub> imputed and missing values were  
1177 replaced with random numbers from a Gaussian distribution with a width of 0.3 and a downshift  
1178 of 1.8. Statistical significance was determined using t-tests. The protein localizations and  
1179 functions were categorized based on the GO term listed below. GO:0006914 (Autophagy),  
1180 GO:0000502 (Proteasome), GO:0009507 (Chloroplast), GO:0005739 (Mitochondria),  
1181 GO:0005777 (Peroxisome), GO:0005840 (Ribosome), GO:0009941 (Chloroplast envelope),  
1182 GO:0009570 (Chloroplast stroma) and GO:0009534 (Chloroplast thylakoid).

1183 **Supplemental Table 10:** Comparison of protein abundances between WT and the *nbr1 atg7*  
1184 double mutant under HL conditions. Analysis was performed using the Perseus platform 2.0.6.0  
1185 (Tyanova et al., 2016), intensity values from mass spectrometry were log<sub>2</sub> imputed and missing  
1186 values were replaced with random numbers from a Gaussian distribution with a width of 0.3 and  
1187 a downshift of 1.8. Statistical significance was determined using t-tests. The protein localizations  
1188 and functions were categorized based on the GO term listed below. GO:0006914 (Autophagy),

1189 GO:0000502 (Proteasome), GO:0009507 (Chloroplast), GO:0005739 (Mitochondria),  
1190 GO:0005777 (Peroxisome), GO:0005840 (Ribosome), GO:0009941 (Chloroplast envelope),  
1191 GO:0009570 (Chloroplast stroma) and GO:0009534 (Chloroplast thylakoid).

1192 **Supplemental Table 11:** Comparison of protein abundances between WT and the *atg7* mutant  
1193 under LL conditions. Analysis was performed using the Perseus platform 2.0.6.0 (Tyanova et  
1194 al., 2016), intensity values from mass spectrometry were log<sub>2</sub> imputed and missing values were  
1195 replaced with random numbers from a Gaussian distribution with a width of 0.3 and a downshift  
1196 of 1.8. Statistical significance was determined using t-tests. The protein localizations and  
1197 functions were categorized based on the GO term listed below. GO:0006914 (Autophagy),  
1198 GO:0000502 (Proteasome), GO:0009507 (Chloroplast), GO:0005739 (Mitochondria),  
1199 GO:0005777 (Peroxisome), GO:0005840 (Ribosome), GO:0009941 (Chloroplast envelope),  
1200 GO:0009570 (Chloroplast stroma) and GO:0009534 (Chloroplast thylakoid).

1201 **Supplemental Table 12:** Comparison of protein abundances between WT and the *nbr1* mutant  
1202 under LL conditions. Analysis was performed using the Perseus platform 2.0.6.0 (Tyanova et  
1203 al., 2016), intensity values from mass spectrometry were log<sub>2</sub> imputed and missing values were  
1204 replaced with random numbers from a Gaussian distribution with a width of 0.3 and a downshift  
1205 of 1.8. Statistical significance was determined using t-tests. The protein localizations and  
1206 functions were categorized based on the GO term listed below. GO:0006914 (Autophagy),  
1207 GO:0000502 (Proteasome), GO:0009507 (Chloroplast), GO:0005739 (Mitochondria),  
1208 GO:0005777 (Peroxisome), GO:0005840 (Ribosome), GO:0009941 (Chloroplast envelope),  
1209 GO:0009570 (Chloroplast stroma) and GO:0009534 (Chloroplast thylakoid).

1210 **Supplemental Table 13:** Comparison of protein abundances between WT and the *nbr1 atg7*  
1211 double mutant under LL conditions. Analysis was performed using the Perseus platform 2.0.6.0  
1212 (Tyanova et al., 2016), intensity values from mass spectrometry were log<sub>2</sub> imputed and missing  
1213 values were replaced with random numbers from a Gaussian distribution with a width of 0.3 and  
1214 a downshift of 1.8. Statistical significance was determined using t-tests. The protein localizations  
1215 and functions were categorized based on the GO term listed below. GO:0006914 (Autophagy),  
1216 GO:0000502 (Proteasome), GO:0009507 (Chloroplast), GO:0005739 (Mitochondria),  
1217 GO:0005777 (Peroxisome), GO:0005840 (Ribosome), GO:0009941 (Chloroplast envelope),  
1218 GO:0009570 (Chloroplast stroma) and GO:0009534 (Chloroplast thylakoid).

1219 **Supplemental Table 14:** Primers used for genotyping.

1220 **Supplemental Data:** Data used for all graphs presented in this study.

1221 **Figure 2G source data:** Original files of full raw unedited blots and figure with uncropped blots.

1222 **Figure 2-figure supplement 1:** Original files of full raw unedited blots. Uncropped blots are  
1223 shown in Fig.2-figure supplement 1.

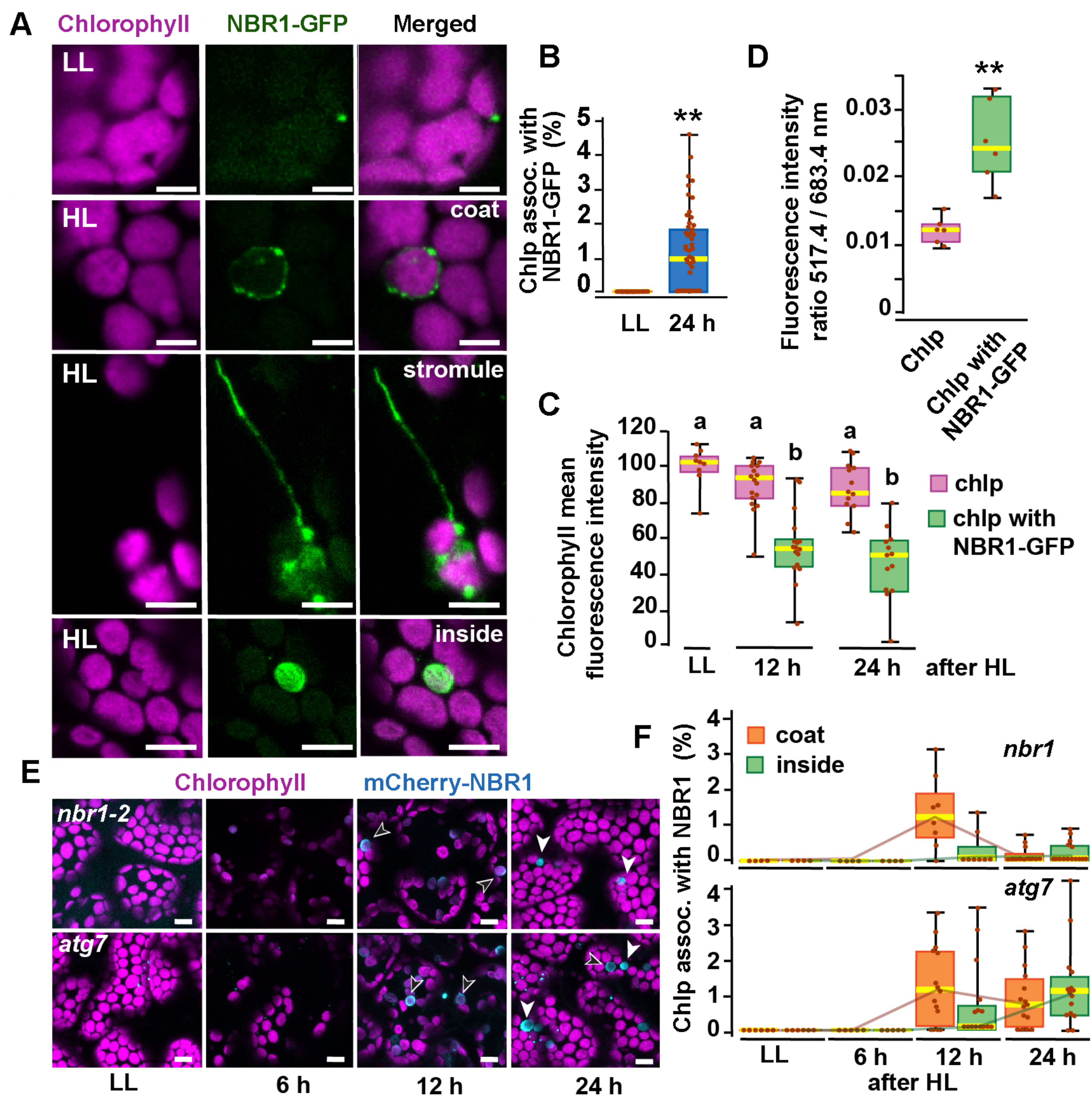


Figure 1

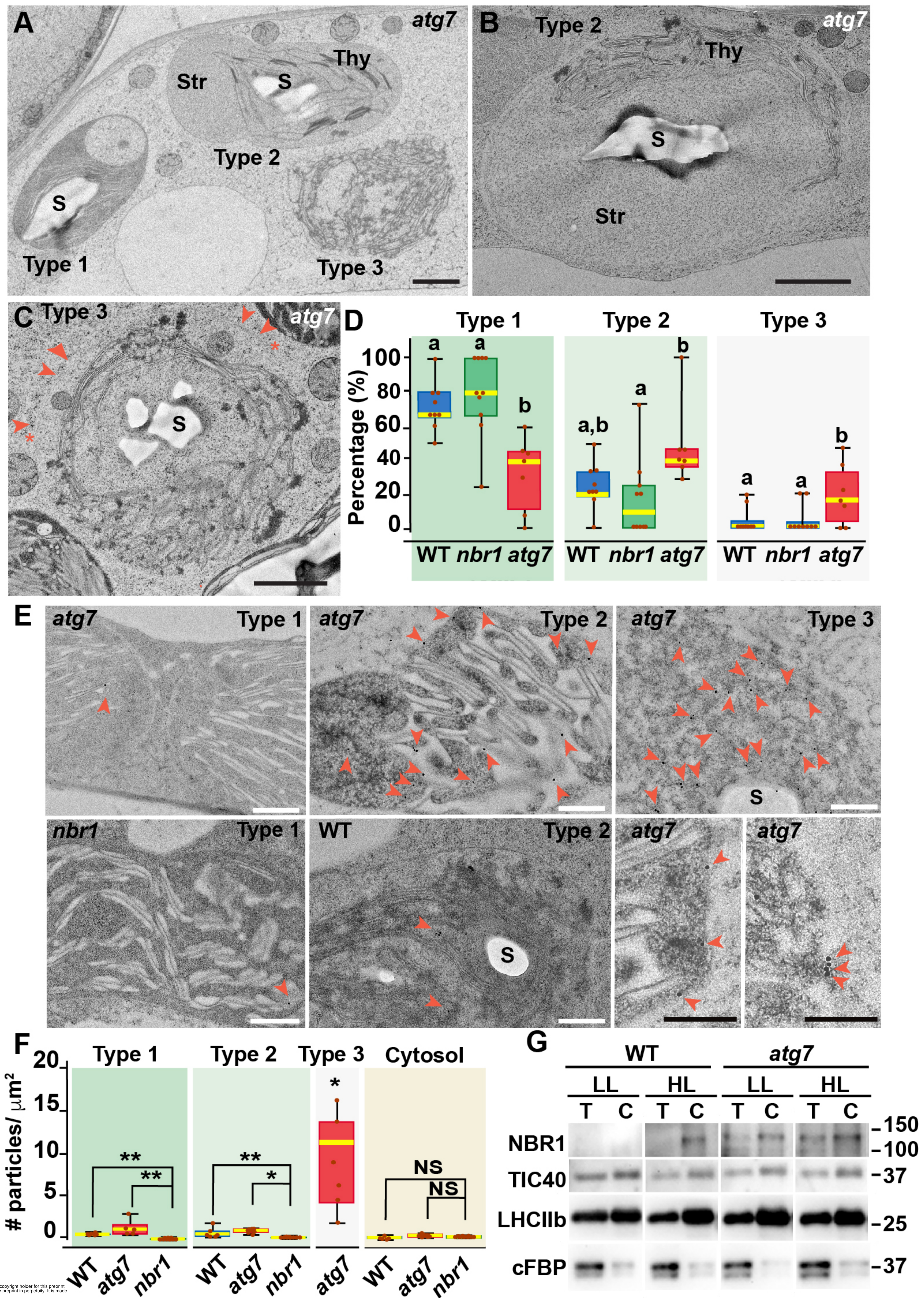


Figure 2

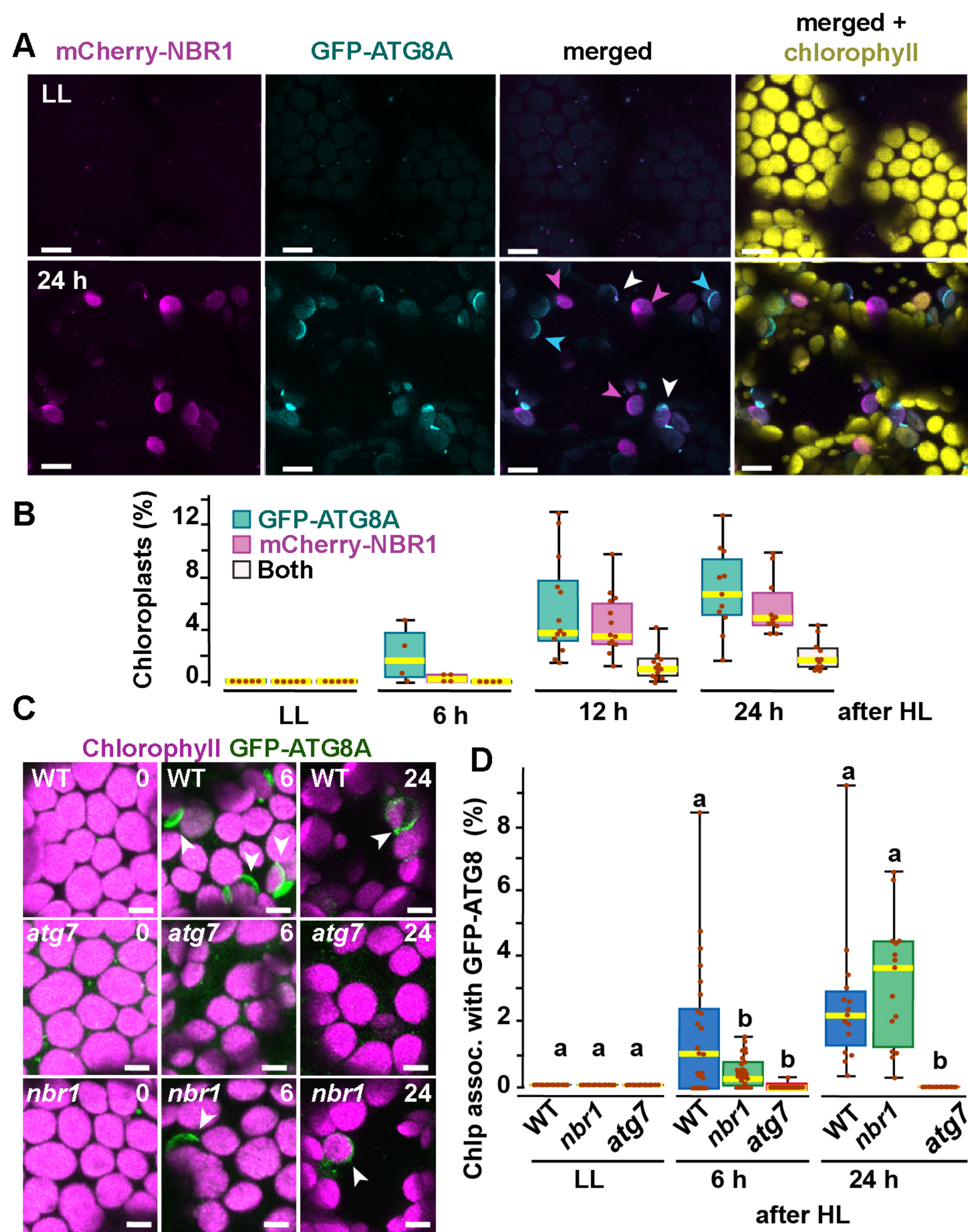


Figure 3



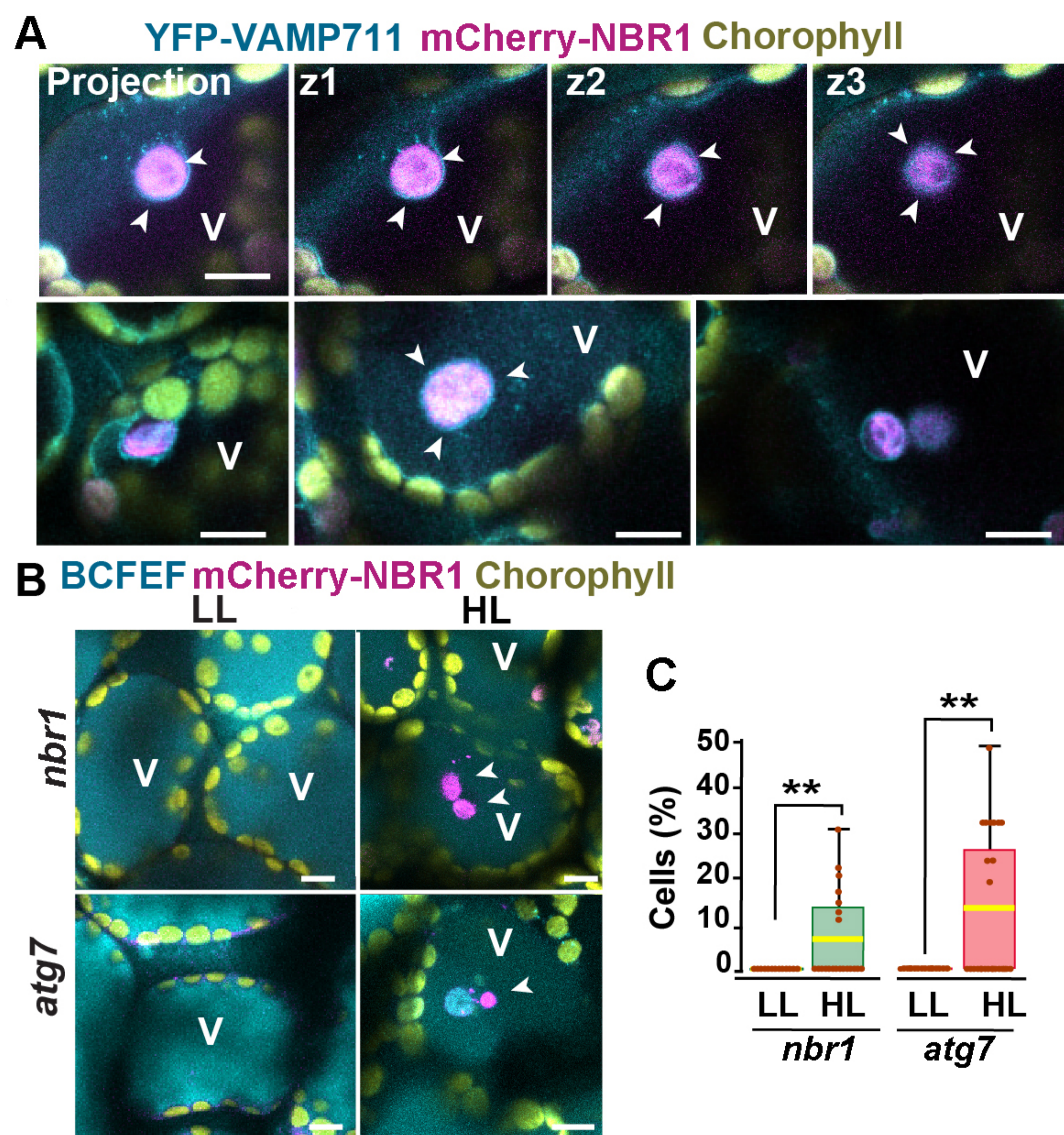


Figure 4

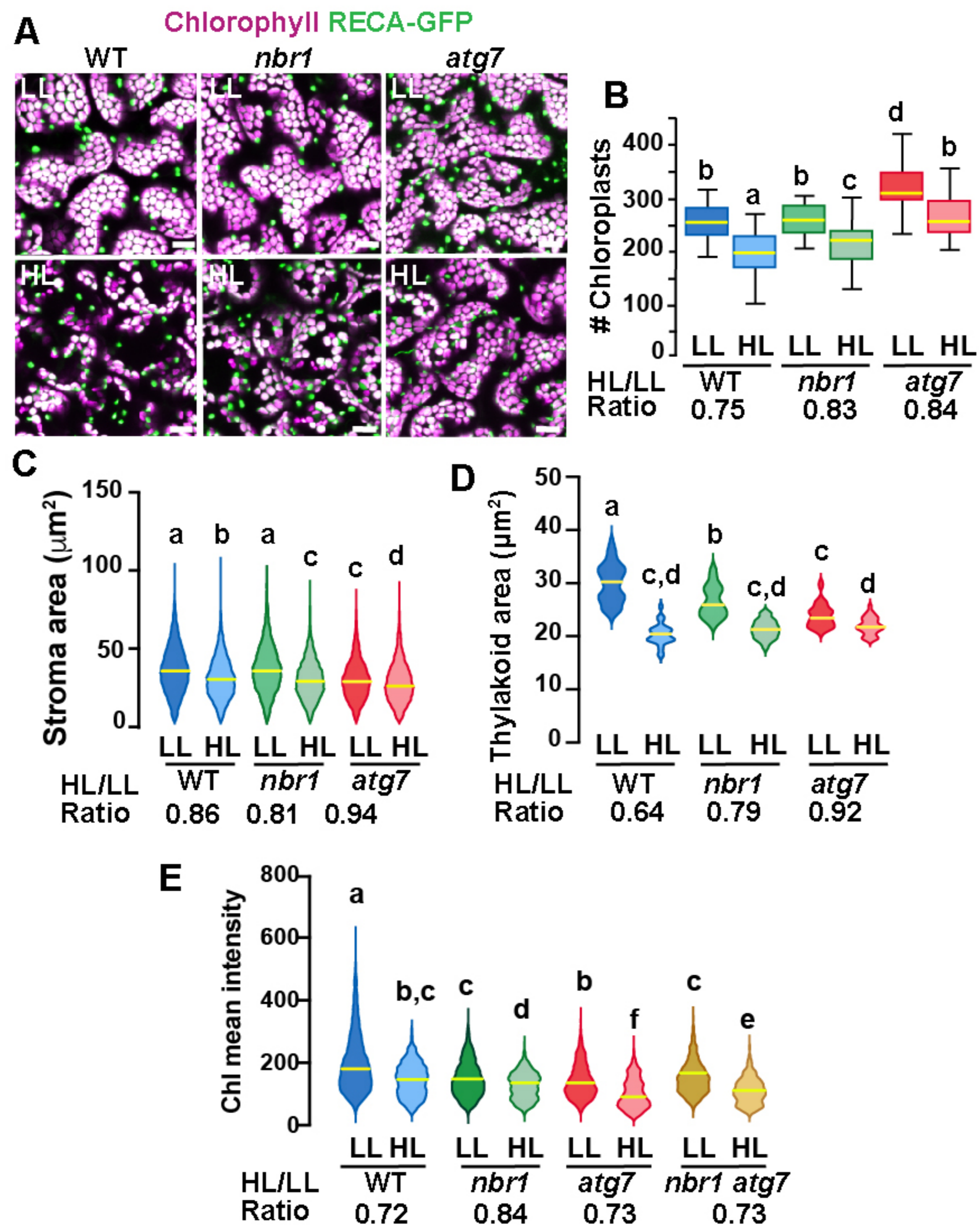


Figure 5

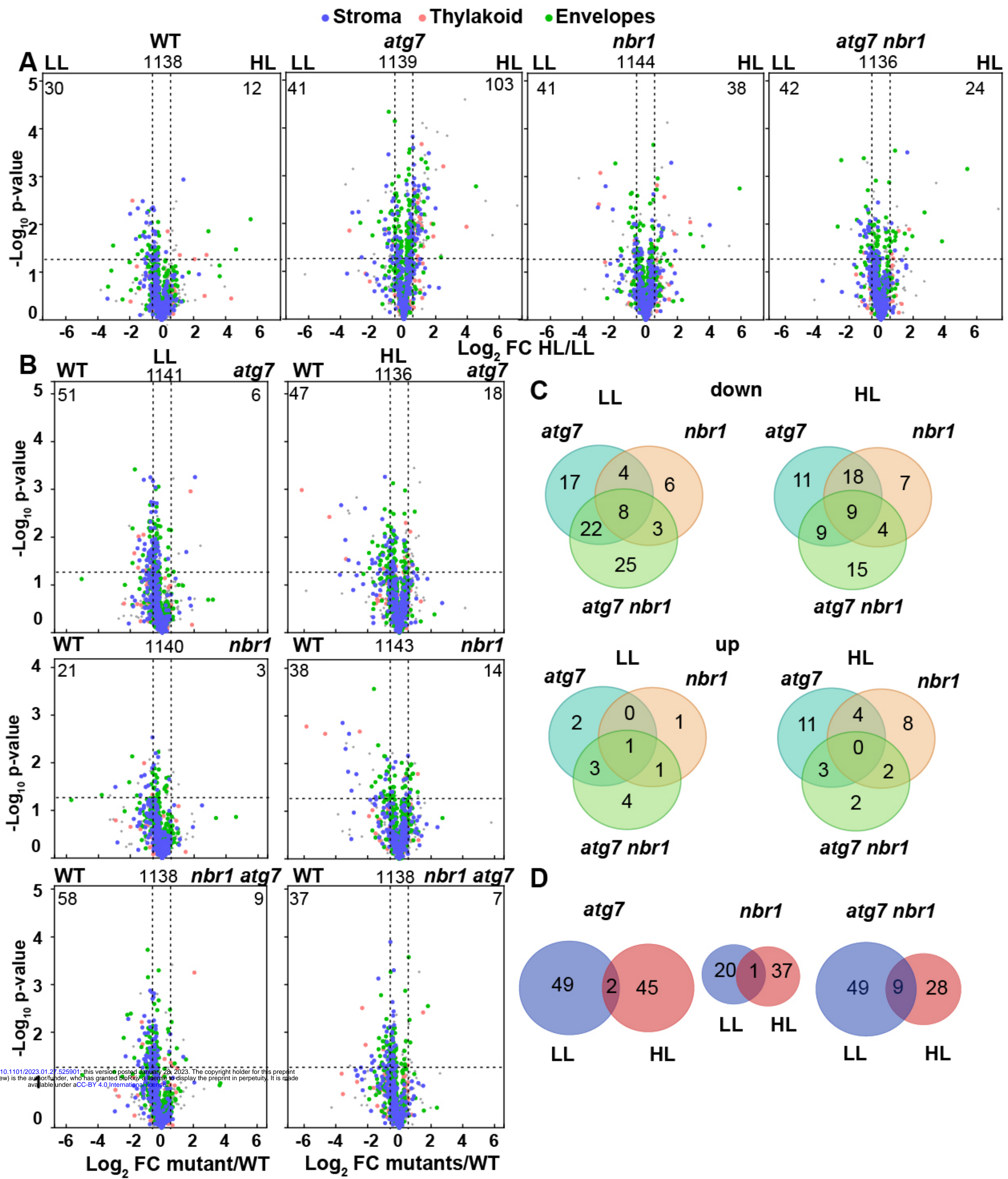


Figure 6

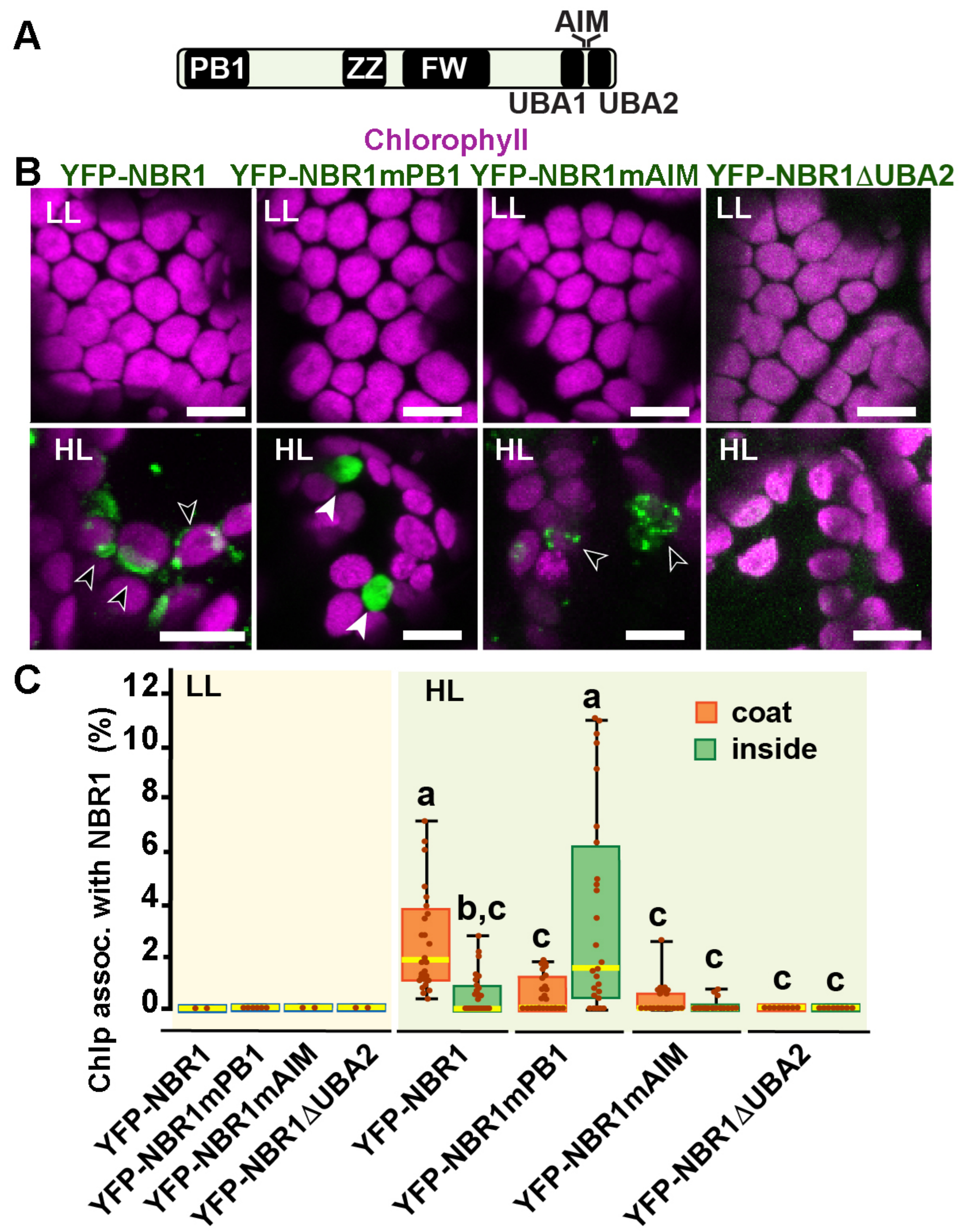


Figure 7

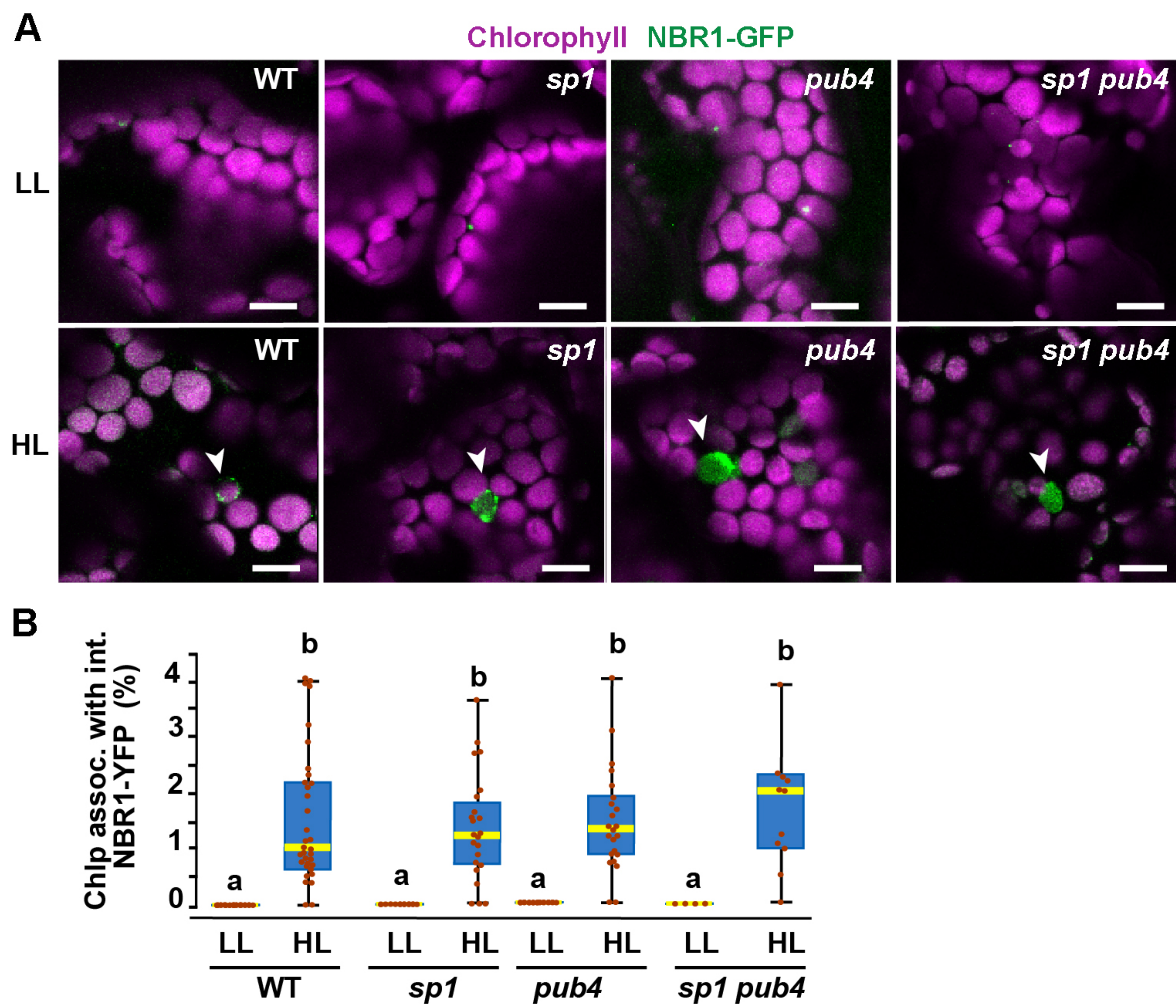


Figure 8

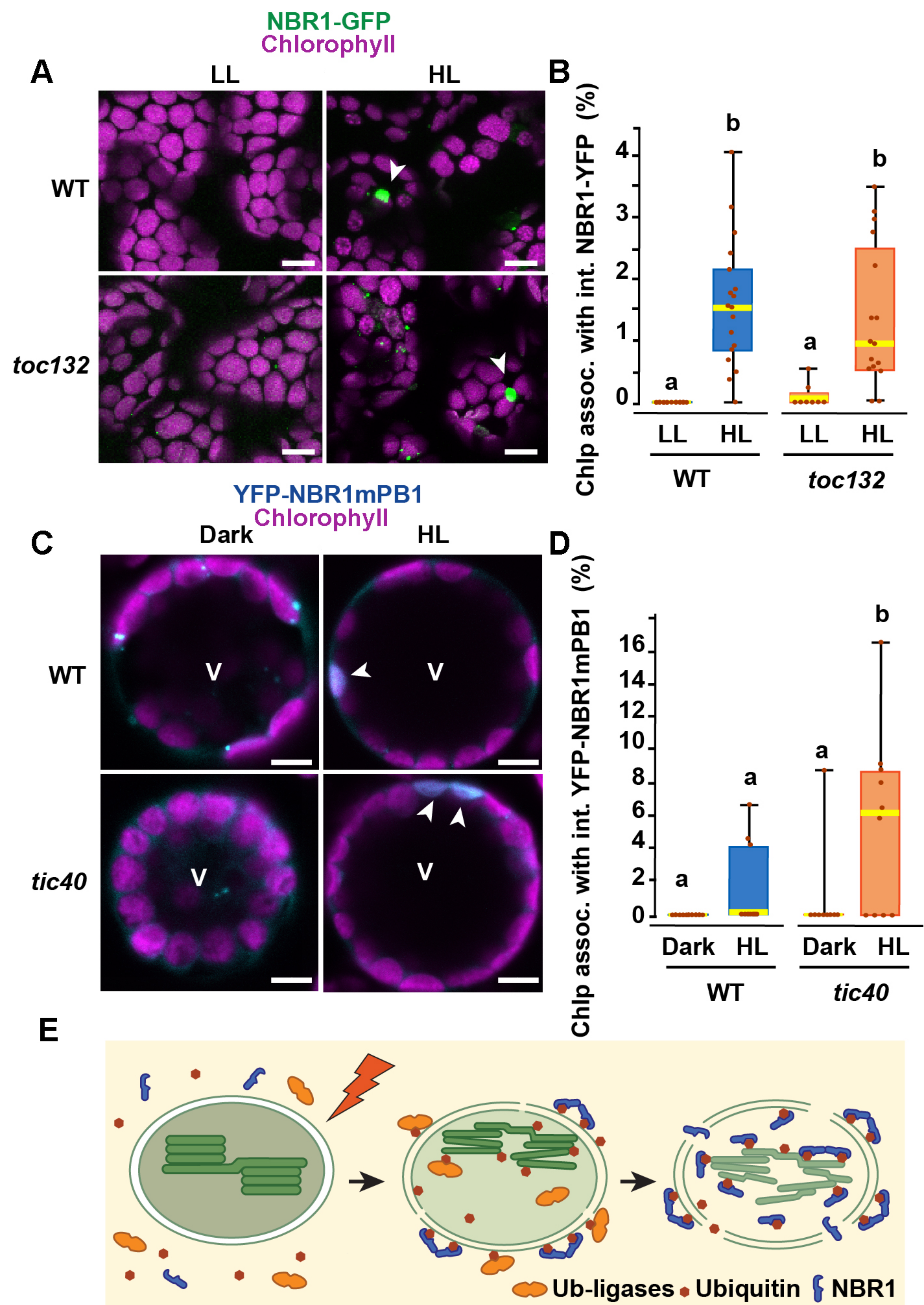
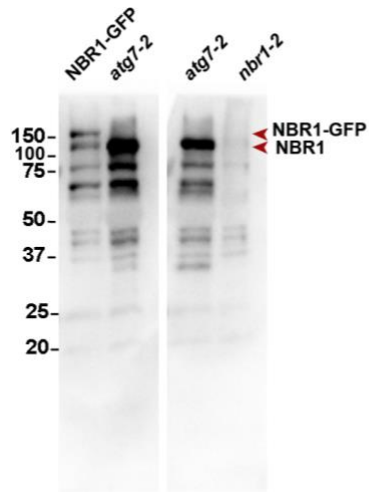


Figure 9

Supplemental Figures  
Lee et al



**Figure 2-figure supplement 1:** Uncropped immunoblot of total proteins from wild type plants expressing NBR1-GFP, and *atg7-1* and *nbr1* mutants using anti-NBR1 antibodies (Jung et al., 2020).

Supplemental Figures  
Lee et al

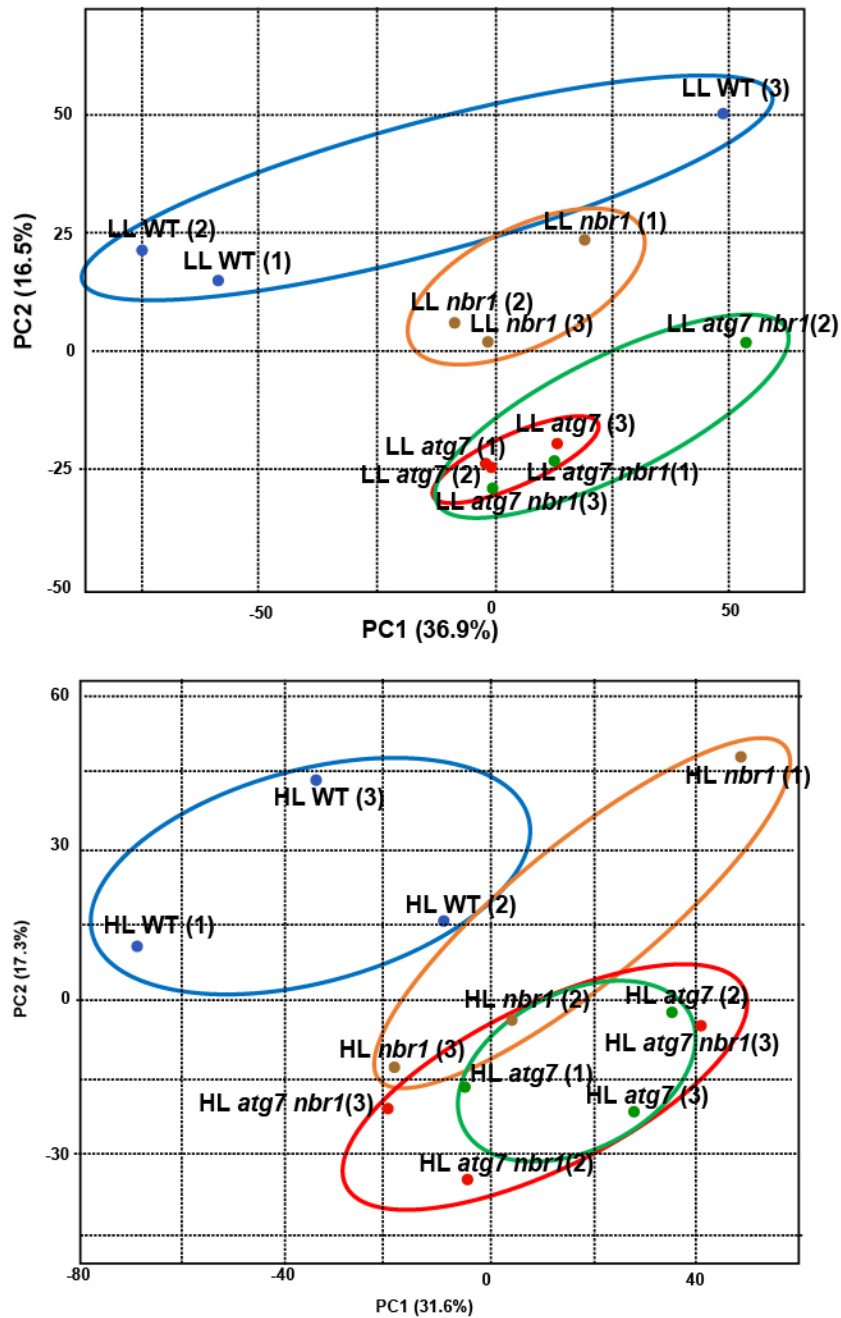


**Figure 6-figure supplement 1: Principal component analysis (PCA) of proteomic analysis samples.** The plot depicts each biological replicate used for the proteomic analysis from WT Col-0, *atg7*, *nbr1* and *nbr1 atg7* plants either under LL or after HL exposure.



Supplemental Figures  
Lee et al

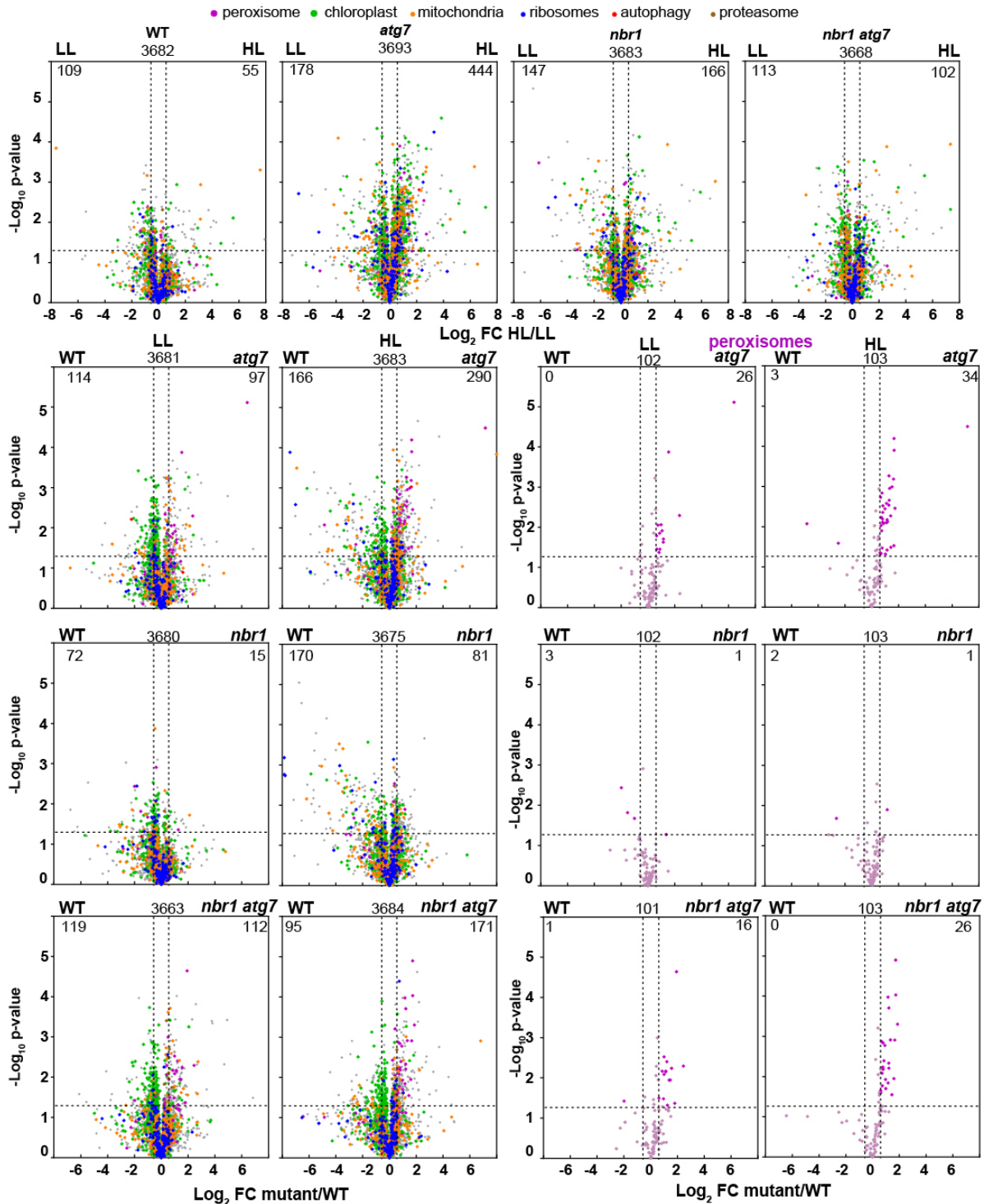


**Figure 6-figure supplement 2: Proteome analysis by liquid chromatography-tandem mass spectrometry (LC-MS/MS).**

**(A)** Volcano plots showing the relative abundance changes of total selected protein in wild type (Col-0), *nbr1*, *atg7*, and *nbr1 atg7* seedlings grown either under LL or exposed to HL and let

## Supplemental Figures

Lee et al

recover for 24 h. Proteins were identified by LC-MS/MS, and their average abundances were calculated from the MS1 precursor ion intensities. Only proteins with at least two peptide spectral matches were considered in the analysis. Each protein is plotted based on its  $\text{Log}_2$  FC in abundance (HL/LL) and its  $-\log_{10}$   $p$ -value in significance based on the three biological replicates.

**(B)** Volcano plots showing the relative abundance changes of total selected protein in mutants compared to wild type (Col-0) either under different light conditions.

**(C)** Volcano plots showing the relative abundance changes of peroxisomal protein in mutants compared to wild type (Col-0) either under different light conditions.

Supplemental Figures  
Lee et al

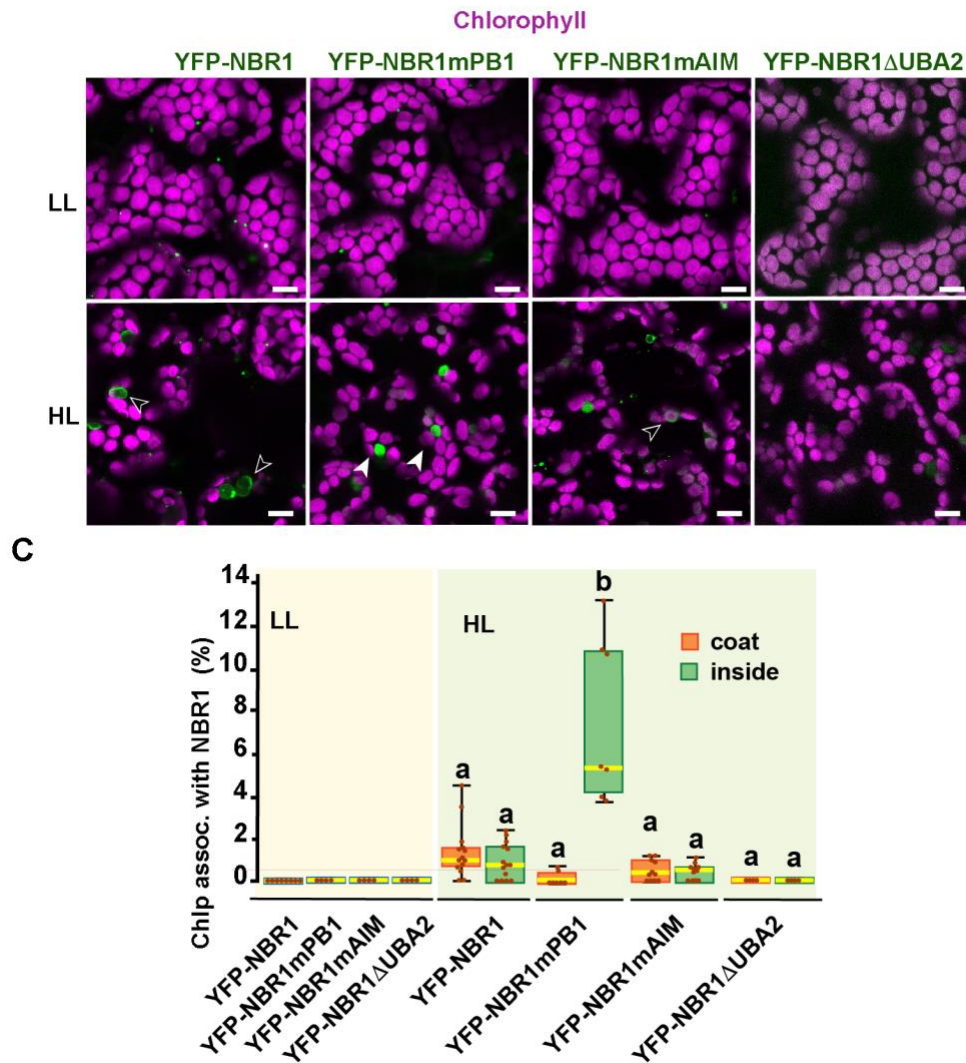


**Figure 7-figure supplement 1: NBR1 domains in NBR1 recruitment to chloroplasts in *nbr1 atg7* double mutant cotyledons after HL treatment.**

**(A)** Confocal imaging of NBR1 mutated proteins fused to YFP expressed in 8-day old *nbr1 atg7* seedlings grown under LL (top) or 24 h after HL exposure (bottom). Hollow arrowheads and filled arrowheads indicate YFP-NBR1 coating chloroplasts and inside chloroplasts, respectively.

**(C)** Box and whisker plots show the percentage of chloroplast associated with the YFP-labeled mutated NBR1 proteins, localized to either coats (orange) or inside chloroplasts (green). Boxes show the variation in data through quartiles; the middle line indicates the median and whiskers show the upper and lower fences.

Scale bars: 10  $\mu$ m in A.